ACS APPLIED MATERIALS & INTERFACES

Open Access

This article is licensed under CC-BY 4.0

www.acsami.org

Research Article

The Three-Component Problem: Deconvoluting Electrolyte Component Roles in Solvation Structure and Silicon Calendar Aging

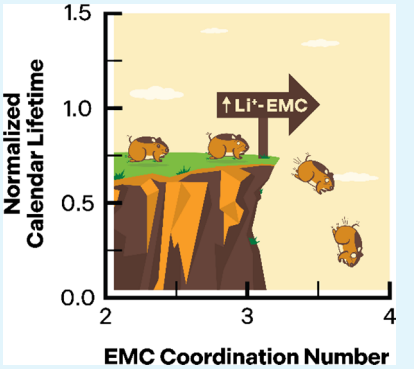
Steven Lam, Nessa Majaya, Kevin L. Gering, Robert L. Sacci, Lydia Meyer, Ankit Verma, Maxwell C. Schulze, Lily A. Robertson, Zhengcheng Zhang, Marco-Tulio Fonseca Rodrigues, Stephen E. Trask, Andrew M. Colclasure, Kristin A. Persson, and Gabriel M. Veith*

Cite This: *ACS Appl. Mater. Interfaces* 2026, 18, 52238–52252

Read Online

ACCESS | Metrics & More | Article Recommendations | Supporting Information

ABSTRACT: In this work, we deconvolute the roles of $LiPF_6$, ethyl methyl carbonate (EMC), and vinylene carbonate (VC) in the electrolyte solvation structure and silicon anode calendar aging. By varying the mole fractions of the electrolyte constituents and utilizing a voltage hold protocol, we extract the roles of each component in the silicon anode calendar lifetime. Interestingly, the $LiPF_6$ concentration does not affect calendar aging, whereas increasing and decreasing the EMC and VC mole fractions, respectively, lowers the electrode surface passivity. The calendar lifetime results align with EMC coordination numbers derived from MD simulations, which indicate the inner solvation sheath's role in calendar aging mechanisms. X-ray photoelectron spectroscopy data show that the solid electrolyte interphase (SEI) species can be tuned through the electrolyte formulation and solvation structure. Li^+-EMC coordination structures decompose to form insoluble alkanes, C−O species, and lithium carbonate (Li_2CO_3), while the anion coordination complex decomposes into LiF and $Li_xPO_yF_z$. Postaging, the surface lithium content of the SEI is partially replaced by C−O species from preferential decomposition of noncoordinated VC. However, the inorganic lithium species (LiF, $Li_xPO_yF_z$, and Li_2CO_3) remain constant, suggesting the dissolution of nonpolar organolithium species due to EMC's low dielectric constant and high coordination number. This triggers continuous electrolyte decomposition to reform the SEI, which lowers the silicon anode's calendar lifetime.



KEYWORDS: *silicon anodes, calendar aging, liquid electrolytes, solvation structure, solid electrolyte interphase*

INTRODUCTION

Silicon (Si) anodes have been extensively explored as a graphite alternative within lithium-ion batteries due to silicon's high specific capacity (3579 mAh g^{-1}).[1] However, time-dependent processes defined as calendar aging limit the commercial viability of Si electrodes.[2] Calendar aging is influenced by the battery condition (e.g., state of charge, storage conditions, and cycling history) and results in open-circuit capacity fade.[2,3] While cycling performance is dictated by mechanical degradation processes (e.g., Si volume expansion and cracking), calendar aging is dominated by chemical degradation mechanisms such as hydrofluoric acid (HF) generation and solid electrolyte interphase (SEI) dissolution.[2,4] The SEI consists of electrolyte decomposition products formed from the battery's initial conditioning steps such as LiF and Li_2CO_3.[5] Stabilizing this passivation layer is crucial in minimizing the Si electrode surface reactivity during calendar aging. Strategies to mitigate aging-related capacity fade such as varying carbon additives (e.g., graphite and C45) and Si functionalization (e.g., vinylene carbonate-milled Si particles) have been utilized.[6−8] However, the aging behavior fundamentally stems from the electrolyte–SEI interactions. More specifically, continuous SEI degradation leads to exposed Si electrode surfaces that can result in accelerated SEI growth and densification leading to electrolyte depletion and capacity fade.[9,10] Thus, we must understand the aging mechanisms associated with the SEI and electrolyte to improve shelf life.[2] Among the many common aging mechanisms are (1) dissolution of the SEI and (2) HF generation.

The generation of HF is believed to occur in lithium hexafluorophosphate ($LiPF_6$)-containing electrolytes. Trace amounts of water within the electrolyte or adsorbed on the electrode facilitate $LiPF_6$ hydrolysis and produce HF.[11] The HF then reacts with the silicon dioxide (SiO_2) layer formed on oxidized silicon and generates water. This hydrolytic cycle continues until SiO_2 or $LiPF_6$ is depleted. The HF produced via

Received: November 18, 2025
Revised: August 12, 2026
Accepted: August 12, 2026
Published: September 21, 2026



ACS Publications

© 2026 The Author(s). Published by American Chemical Society

https://doi.org/10.1021/acsami.5c23255
ACS Appl. Mater. Interfaces 2026, 18, 52238–52252

Downloaded from pubs.acs.org/aamick/article-pdf/18/38/52238/6858305O/am-2025-23255a.pdf by LAWRENCE BERKELEY NATL LABORATORY user on 06 November 2026

the hydrolytic cycle etches the SEI and the Si anode, promoting instability during calendar aging.[12,13] However, the direct impact of HF attack on calendar life is still controversial, as Rodrigues et al. revealed that aged Si-graphite/$LiNi_{0.6}Mn_{0.2}Co_{0.2}O_2$ composite electrodes showed negligible capacity loss after 4 years of aging at a low state of charge (3 V).[14] The authors argued that the chemical mechanism of HF attack would be exhibited more readily at low-capacity storage due to its non-dependence on anode potential. Additionally, the solvents may play a role in $LiPF_6$ hydrolysis kinetics.[15] Stich et al. found that the HF concentration of a 1 M $LiPF_6$ in EC/dimethyl carbonate (50:50, vol/vol) with 70 mmol L^{-1} H_2O reached approximately 95 mmol L^{-1} after 14 days.[16] However, they observed negligible amounts of HF in an aqueous $LiPF_6$ electrolyte (0.1 mmol L^{-1}), indicating that the organic solvents accelerated HF production. Therefore, the direct link between water contamination, HF etching, and calendar life has still not been conclusively demonstrated.

In addition to HF attack during calendar aging, the organic solvents (e.g., ethylene carbonate (EC) and ethyl methyl carbonate (EMC)) within the electrolyte may dissolve the SEI and expose bare Si promoting electrolyte decomposition.[17] Sayavong et al. observed SEI dissolution with varying electrolyte formulation via in-operando electrochemical quartz crystal microbalance.[18] They found that increasing the LiFSI concentration from 0.5 M to 4 M in a 1,2-dimethoxyethane (DME) solvent decreased SEI mass loss from dissolution from 60% to 7%. This is most likely due to lower organic solvent content in the electrolyte that would induce SEI dissolution. The varying rates of dissolution could be explained by the solvent dielectric constants where a higher dielectric constant would lead to increased SEI mass loss. Additionally, SEI components each inherently possess varying solubilities, which play a role in the rate of dissolution.[19] Tasaki et al. performed studies on the solubility of different inorganic and organic lithium salts at 25 °C that are typically present in the SEI. They found that organic salts such as lithium ethylene dicarbonate (LiEDC) (heat of dissolution, ΔH_{diss} = –21.65 kcal mol^{-1}) possess higher solubilities than the inorganic salts such as lithium oxide (Li_2O) (ΔH_{diss} = 42.66 kcal mol^{-1}).[20,21] Furthermore, the organic salt showed increased solubility in EC compared to dimethyl carbonate (DMC), as compared to EC, where the ΔH_{diss} of LiEDC shifted from –21.65 to –14.04 kcal mol^{-1}. This was attributed to the higher polarity of EC compared to that of DMC, where the dielectric constants for each solvent are 89.6 and 3.12, respectively. This implies that the SEI species solubilities are linked to the solvent dielectric constants. More specifically, low-polarity organic lithium salts dissolve more readily in low dielectric solvents than the inorganic salts. Overall, these works show the importance of understanding the link between electrolyte constituents and calendar aging.

Prototypical electrolytes consist of lithium salt and a few solvents, most commonly carbonates. While the standard Gen2 electrolyte (1.2 M $LiPF_6$ in 3:7 wt:wt EC/EMC) has been widely studied in Li-ion batteries with graphite anodes, poor surface passivation of the Si anode accelerates capacity fade during calendar aging.[22−24] Malkowski et al. performed a multicomponent analysis on the Gen2 electrolyte. They revealed that increased PF_6^- and EC coordination is detrimental to calendar lifetime due to increased parasitic currents during V-hold experiments.[25] Furthermore, the substitution of EC with other solvents such as propylene carbonate (PC) stabilized the SEI lithium complexes and improved calendar life. Similarly, Verma et al. replaced the EMC solvent in the Gen2 electrolyte with fluoroethylene carbonate (FEC) electrolyte. Compared to the traditional electrolyte, the 1.5 M $LiPF_6$ in EMC:FEC (9:1 w/w) increased the calendar lifetime by 400%.[22] During a 13-week open circuit potential rest, plasma-focused ion beam tomography performed by Quinn et al. revealed lithium fluoride (LiF) growth at the current collector-electrode interface from FEC reduction.[26] The LiF growth resulted in delamination of the Si anode and loss of active material that could be detrimental to calendar life. Substituting the Gen2 electrolyte for other electrolyte formulations has shown improvements in Si surface passivity.[27]

Within the electrolyte, lithium cations in electrolyte coordinate with the salt anions and solvent molecules, forming a solvation sheath composed of ion–ion and ion–dipole interactions. The thermodynamically driven proportions of these solvating members in cation solvation sheaths will depend in part on electrolyte attributes, such as the bare ionic radii, salt concentration, donor number, and solution permittivity at conditions of operation.[28] The first solvation structure is defined as the species directly coordinated with the Li^+ and is commonly categorized as three types: contact-ion pairs (CIPs), solvent-separated ion pairs (SSIPs), and aggregates (AGGs). In the presence of a potential gradient, the Li^+ is transported to the electrode surface in the solvation sheath via a shuttling mechanism. As the cation approaches the surface of the Si anode, the solvation sheath is stripped away.[29] The anions and solvent species stripped during the shuttling process can undergo reduction on the electrode surface to form the SEI.[30,31] For prototypical electrolyte systems, all constituents typically play a role in the inner solvation sheath. For example, in the Gen2 electrolyte, Hou et al. performed molecular dynamics (MD) simulations to find the coordination numbers (N) for the PF_6^- anion (N_{PF6-} = 0–1), EC (N_{EC} = 1–2.5), and EMC (N_{EMC} = ∼3) and indicated that EMC is the dominating species within the first solvation sheath.[31] Additives can also alter the solvation structure. Additional MD simulations performed by Hou et al. discovered that the addition of 10 wt % FEC to 1.0 M $LiPF_6$ in EC significantly resulted in a notably higher CIP ratio of 14% relative to the 6% with no additive.[30] The FEC additive was found to participate in 19% of the first coordination shells. In agreement, He et al. explored quantum chemical calculations and found that in $LiPF_6$ in PC with varying additives such as vinylene carbonate (VC), FEC, and vinyl ethylene carbonate, the additives possessed coordination numbers of ∼3.1 resulting in additive-derived SEIs.[32] Overall, although the electrolyte constituents dictate the species that exist in the electrolyte–SEI interface, the relationship between the solvation structure and surface stability of Si has yet to be completely elucidated.

In this study, we prepare 17 $LiPF_6$:EMC:VC electrolyte formulations to examine the interplay between the electrolyte constituents, coordination structure, and Si anode calendar lifetime. The $LiPF_6$:EMC:VC electrolyte system is chosen based on work performed by Woods et al. where the authors incorporated VC as a cosolvent rather than an additive.[33] A 1.2 M $LiPF_6$ in EMC:VC (10:2 w/w) exhibited improved capacity retention (∼750 mAh g^{-1}) for 950 cycles, whereas the Gen2 with 3 wt % FEC (Gen2F) and 1.2 M $LiPF_6$ in EMC:VC (10:1 w/w) reached cell death (∼0 mAh g^{-1}) at approximately 300 cycles. These findings corroborate with other studies, which

Downloaded from pubs.acs.org/aamick/article-pdf/18/38/52238/6858050/am-2025-23255a.pdf by LAWRENCE BERKELEY NATL LABORATORY user on 06 November 2026

https://doi.org/10.1021/acsami.5c23255
ACS Appl. Mater. Interfaces 2026, 18, 52238−52252

indicate that incorporation of VC leads to promising cycle life and calendar aging performance.[34,35] Indeed, for graphite anodes, Geuder et al. showed that by adding 5 wt % VC to a $LiPF_6$, EC, and EMC electrolyte, the relative capacity loss decreased from approximately 16% to 9% after 5.5 months of aging.[36] This may be attributed to the better passivation properties derived from the VC-based polymeric SEI.[37] However, excessive VC content led to SEI thickening and increased cell impedance.[38,39] These studies have primarily explored the role of VC additive for graphite anode cycling performance. For Si electrodes, we utilize a V-hold protocol to deconvolute the $LiPF_6$, EMC, and VC roles during aging. The parasitic reactions that occur during calendar aging are linked to the residual currents measured during the V-hold protocol. By fitting this residual current profile, we extract the estimated calendar lifetimes and connect this to the coordination structure, SEI composition, and ionic conductivity as a function of electrolyte composition.

EXPERIMENTAL METHODS

Electrode Fabrication

Si powder was produced by pulverizing a Si boule in a rock crusher into a <10 mesh powder. The <10 mesh Si powder, 3/32″ 440C milling media (Union Process), and PC (Sigma-Aldrich-Millipore, 99.7%) were loaded in a 7:52:8 (Si:media:PC) ratio into a 125 mL stainless-steel mill jar (Retsch eMax mill). This mixture was milled at 1500 rpm for 8 min followed by a 20 min cool down PC and repeated 5 times. PC is utilized to minimize postmilling aggregation and to passivate the Si surface. We removed excess PC by drying the milled slurry at 250 °C for 2 h. This drying process has been shown to produce covalently bound carbon species on the Si surface that may improve Li^+ transport.[6]

Separately, we prepared a 10 wt % P84 polyimide (Tecapowder) in *N*-methyl-2-pyrrolidone (NMP, BeanTown Chemical, >99%) solution. The electrode slurry was composed of the in-house PC-milled Si, C45 carbon black (TIMCAL Super C45), and P84 (in 80:10:10 wt %). The slurry components were mixed in a 20 mL polyethylene bottle with 5 mm beads of yttria-stabilized zirconia milling media via a Turbula mixer for 1 h. After mixing, the Si slurry was doctor bladed onto copper foil (MSE Supplies, battery grade, 12 μm thickness) with a wet gap of 25 or 100 μm, depending on the desired areal capacity. The NMP solvent was removed by drying the wet electrodes on a hot plate at 100 °C. We further dried the electrodes at 90 °C under vacuum to remove excess moisture and prevent copper oxidation during the curing process. Once dried, the electrodes were cured at 350 °C with a 10 °C min^{-1} ramp rate for 1 h under an argon environment. The average areal mass loadings of the 25 and 100 μm blade gap electrodes were 0.19 and 1.07 mg_{Si} cm^{-2}, respectively. The 25 μm wet gap electrode loading was designed to probe surface passivity in full cells containing excess lithium inventory. The 100 μm-thick Si electrodes were utilized for *ex situ* X-ray photoelectron spectroscopy (XPS).

Electrolyte Formulation

Prior to electrolyte mixing, we performed a single-stage vacuum distillation of the VC (Sigma-Aldrich-Millipore, battery grade) to remove the stabilizing agent. The $LiPF_6$ (Chameleon Reagent, battery grade) salt was dried at 90 °C under vacuum overnight. The VC and EMC (Sigma-Aldrich-Millipore, >99%) were mixed with molecular sieves (4Å) and allowed to dry overnight at room temperature. All electrolyte solutions were made in a dry room environment (dew point ≈ −70 °C). Electrolyte compositions containing observable undissolved $LiPF_6$ salt after 5 days were classified as insoluble formulations. All electrolyte solutions were stored in a refrigerator within the dry room to inhibit VC polymerization.

Electrochemical Tests

Lithium iron phosphate (LFP) and in-house fabricated Si electrodes were used as the cathode and anode, respectively. The LFP cathodes contained 3.9% C45 carbon additive (Timcal), 0.1% single-walled carbon nanotubes (Tuball), 92% LFP (Johnson Matthey), and 4.0% polyvinylidene fluoride binder (Solvay 5130) by weight. These LFP electrodes were manufactured at Argonne National Laboratory's Cell Analysis, Modeling, and Prototyping (CAMP) Facility. We dried the anode and cathodes in a vacuum oven at 90 °C for at least 12 h to remove excess moisture. To guarantee sufficient lithium inventory during the V-hold experiment, the LFP cathode's areal capacity (3.4 mAh cm^{-2}) was larger than the Si anode's areal capacity (~0.68 mAh cm^{-2}). Coin cells (CR2032, stainless steel with polypropylene gasket) were fabricated in a dry room environment. 19 mm-diameter Celgard 2325 separators were dried at room temperature under dynamic vacuum for ≥24 h. The N/P ratio of the electrodes was 0.2 while the Si anode and LFP cathode diameters were 14 and 15 mm, respectively. We assembled the coin cells by first dispensing 20 μL of electrolyte on the anode. We then placed the separator atop the anode, dispensed an additional 40 μL of electrolyte, and placed the cathode on the separator. Finally, the coin cell was sealed. To ensure proper electrode wetting, we let each coin cell rest for 4 h. The calendar life test consisted of two steps: (1) SEI formation and (2) a 500 h potential hold to monitor parasitic currents during calendar aging. For the formation step, the 4 h rest period was followed by two C/10 cycles from 2.7 to 3.4 V, a charge to 3.4 V, and then the cells were held a "wetting" voltage hold at 3.4 V for 40 h (Maccor 4000). The cell was then discharged at C/10 to 2.7 V followed by 10 C/3 cycles from 2.7 to 3.4 V. This conditioning step was followed by the V-hold protocol to assess calendar life. The cell was cycled at C/10 three times between 2.7 and 3.4 V, charged to 3.4 V, and held for 500 h. After the hold, the cells were cycled at C/10 three times. After all discharge steps during the V-hold protocol, a constant current, constant voltage step was performed at 2.7 V to remove silicon hysteresis as a variable. Each electrolyte formulation was tested in triplicates to ensure reproducibility.

We measured the ionic conductivity for each electrolyte formulation with a Pt dip conductivity cell (Cole-Parmer) in a dry room environment. A 1.413 mS cm^{-1} conductivity standard (Mettler Toledo) was used to determine the cell constant (k = 1.05 cm^{-1}) in air at room temperature. Prior to each measurement, the dip probe was rinsed with the following procedure to remove excess solvent and electrolyte: EMC, DMC, EMC, and then dried. The probe was allowed to soak for at least 3 min in each electrolyte. We performed electrochemical impedance spectroscopy (Biologic VMP-3e) to extract the ionic conductivity from the high-frequency intercept via the following equation (eq 1):

$$\sigma_{\text{Electrolyte}} = \frac{k}{R_{\text{Bulk}}} \tag{1}$$

where R_{bulk} and k are the high-frequency resistance and cell constant, respectively. The frequency range was 200 kHz to 100 mHz with a potential amplitude of 10 mV.

Voltage Hold Fitting

The V-hold modeling and parameter estimation have been discussed in previous works.[22,24] Figure 1 (green region) shows an example of the conditioning step with C/10 formation step, 40 h V-hold at 3.4 V, and C/3 cycling procedure. We note that the conditioning step also acts as the SEI formation protocol. The blue region of Figure 1 shows a C/10 SEI formation step followed by a 500 h V-hold at 3.4 V and C/10 cycling procedure. The nominal capacity and capacity exchanged before, after, and during the V-hold are defined as. Q_{nom}, Q_1, Q_2, and Q_{hold}, respectively. The residual current profile observed during

Downloaded from pubs.acs.org/aamick/article-pdf/18/38/52238/6858050/am-2025-23255a.pdf by LAWRENCE BERKELEY NATL LABORATORY user on 06 November 2026

https://doi.org/10.1021/acsami.5c23255
ACS Appl. Mater. Interfaces 2026, 18, 52238−52252

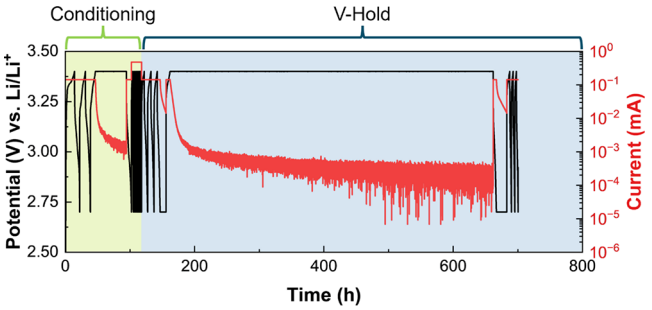


Figure 1. Example of voltage profile during conditioning step (green region) and 500 h V-hold protocol (blue region) for a coin cell containing 0.1:0.72:0.18 (mole fraction) $LiPF_6$:EMC:VC electrolyte. The oversized cathode was LFP. Data fitting was performed to extract calendar aging parameters.

the V-holds are depicted by the red lines. The capacity during the V-hold is defined as the sum of the irreversible (Q_{irrev}) and reversible (Q_{rev}) capacities (eqs 2 and 3):

$$Q_{hold}(t) = Q_{rev}(t) + Q_{irrev}(t) = \frac{Q_{rev}^{final}(c + t_{final})t}{t_{final}(c + t)} + at^p \quad (2)$$

$$Q_{hold}^{final} = Q_{rev}^{final} + Q_{irrev}^{final} \quad (3)$$

Here, $Q_{hold}{}^{final}$, $Q_{rev}{}^{final}$, and $Q_{irrev}{}^{final}$ are the cumulative hold, reversible, and irreversible capacities at the end of V-hold time duration (t_{final} = 500 h), respectively. While the plateauing behavior of reversible Si lithiation is reflected in Q_{rev}, Q_{irrev} displays a power law dependence on time.[40,41]

Capacities in the charge and discharge steps before and after the 500 h V-hold, respectively, can be related to the irreversible parasitic capacity and reversible lithiation during calendar aging. Constant current and constant voltage steps postdischarge remove capacity associated with silicon hysteresis as a variable. As described earlier, the oversized cathode (N/P <<1) and flat-cathode open-circuit potential allow excess Li inventory that will compensate for losses due to parasitic SEI reactions. Therefore, the irreversible Li loss to the SEI should not affect cell capacity after V-hold (eq 4):

$$Q_2 = Q_1 + Q_{rev}^{final} \quad (4)$$

If the cell exhibits extreme capacity losses, Li inventory exhaustion can occur, leading to low-cycling capacities such that (eq 5):

$$Q_2 = Q_1 + Q_{rev}^{final} - Q_{irrev}^{final} \quad (5)$$

Finally, the final irreversible capacity can be estimated by (eq 6):

$$Q_{irrev}^{final} = Q_{hold}^{final} - Q_{rev}^{final} = at_{final}^p \quad (6)$$

All fitting has been performed using an in-house Python script.

X-Ray Photoelectron Spectroscopy

For post-SEI formation XPS analysis, the diameters of the Si anode (3.8 mAh cm^{-2}) and LFP cathodes (3.04 mAh cm^{-2}) were 15 and 14 mm, respectively. The coin cell assembly procedure was identical to the V-hold experiment. After a 4 h rest, the coin cells underwent three C/10 SEI formation cycles from 2.9 to 3.8 V. Post-calendar aging analysis was performed on the Si anodes after the V-hold protocol. Immediately after the formation cycles or calendar aging, the cells were disassembled, and the Si anodes were extracted in an argon-filled glovebox. The electrodes were dipped twice in DMC (Sigma-Aldrich, >99%) to remove residual electrolyte then dried in a glovebox antechamber under dynamic vacuum.

XPS was conducted with a SPECS Enviro-ESCA in ultrahigh vacuum mode using a 15 keV monochromatic Al X-ray source. To avoid air contact, electrode samples were prepared in an argon-filled glovebox and transferred to the XPS instrument with a SPECS EnviroESCA vacuum suitcase. We performed charge correction using adventitious carbon (284.8 eV). Peak fitting of the XPS spectra was done via CasaXPS using a Shirley background subtraction and Gaussian fit.

Molecular Dynamics Simulations

All MD simulations were performed through OpenMM[42] using the atomate2[43] workflow and employed the non-polarizable Sage force field.[44]

The molecular geometries of EMC and VC solvents and PF_6^- anion were optimized using density functional theory (DFT) with Q-Chem version 6.[45] Optimization was performed with the ωB97X-V range-separated hybrid generalized gradient approximation exchange-correlation functional and the cc-pVTZ basis set. Following geometry optimization, partial atomic charges were obtained using the RESP method and subsequently assigned to each molecule for use in the classical MD simulations. Atomic partial charges of Li^+ and PF_6^- ions were scaled by a factor of 0.8. Non-polarizable force fields, such as the Sage force field used in these simulations, do not include explicit electronic polarization and tend to overestimate electrostatic interactions. A common correction is to apply charge scaling to account for the missing polarization effects.[46,47]

Initial simulation boxes were constructed using Packmol[48] to randomly distribute solvent molecules and ions according to the desired stoichiometry. Each system contained 300 Li^+ cations and 300 PF_6^- anions, with solvent counts adjusted to maintain the desired composition.

The energy of the systems was first minimized. The systems were then equilibrated in the isothermal-isobaric (NPT) ensemble for 8 ns at 298 K and 1 atm, maintained using the Monte Carlo barostat. This was followed by a 30 ns annealing procedure, which consisted of a 10 ns temperature ramp up from 298 to 400 K, a 10 ns hold at 400 K, and a subsequent 10 ns ramp down to 298 K. Production simulations were then conducted in the canonical (NVT) ensemble for 80 ns at 298 K using the Langevin Integrator thermostat. Periodic boundary conditions were used in all directions.

Solvation structure analyses were performed exclusively on the equilibrated NVT production trajectories using the SolvationAnalysis package,[49] which employs the MDAnalysis Python package.[50,51] A timestep of 1 fs was used. The coordination numbers are obtained from radial distribution functions (RDFs) computed between Li^+ and the coordinating atoms of each species. Specifically, Li−F distances were used for PF_6^- coordination, and Li−O (carbonyl) distances were used for EMC and VC coordination. The coordination number is calculated by integrating the RDF up to the first minimum following the primary peak. The first minimum is automatically identified using the SolvationAnalysis package. In cases where the automated detection was ambiguous, the RDFs were inspected and the first minimum was manually identified. The reported coordination numbers are ensemble averages, computed by averaging over all Li^+ ions and over all frames of the equilibrated production trajectories.

Because absolute coordination numbers derived from nonpolarizable force fields can depend on charge scaling factor, we performed a systematic sensitivity analysis to evaluate the robustness of the EMC coordination descriptor. Additional MD simulations were performed for 13 compositions using charge scaling factors ranging from 0.4 to 1.0. While the absolute coordination numbers shift with charge scaling, the qualitative trends remain unchanged. Across all charge scaling factors, we observe a compositional regime with elevated solvent coordination that correlates with lower calendar life. Detailed coordination values and full sensitivity analysis across scaling factors are provided in the Supporting Information.

Downloaded from pubs.acs.org/aamick/article-pdf/18/38/52238/6858050/am-2025-23255a.pdf by LAWRENCE BERKELEY NATL LABORATORY user on 06 November 2026

https://doi.org/10.1021/acsami.5c23255
ACS Appl. Mater. Interfaces 2026, 18, 52238−52252

Advanced Electrolyte Modeling

As a complement to ab initio techniques described earlier, the advanced electrolyte model (AEM) was employed to investigate correlations between key electrolyte properties and cell calendar aging. AEM is a molecular-based chemical physics (statistical mechanical) computational platform that uses an advanced form of the mean spherical approximation that allows for variable ion solvation, variable solution permittivity (dielectric "constant") over salt concentration, ion association, and temperature effects.[52−54] This is highly applicable to this work as the span of electrolyte formulations cover an appreciable range of ion association and related permittivity behavior. Central to the AEM architecture is an ion solvation equation of state that renders the solvation outcomes for all species in the solution (e.g., free ions, ion pairs, and triple ions) such that a mass continuity condition is satisfied for the solution. From this, solvation numbers and binding energies are determined for each step in salt concentration. The accuracy of AEM has been validated over wide ranges of salt concentration and temperature and used to predict scores of properties for multiple studies involving lithium-ion, sodium-ion, and lithium metal batteries, with some recent cases involving machine learning.[55] We note that for the sake of concise nomenclature herein, "dielectric constant" is used as an umbrella term in place of relative permittivity. Extended discussion of these terms can be found in the Supporting Information.

■ RESULTS AND DISCUSSION

In this study, we prepared 17 formulations of the $LiPF_6$:EMC:VC electrolyte (Figure 2) to explore the role of electrolyte components in Si anode calendar aging as characterized by the V-hold protocol.[22,23] In 13 out of the 17 formulations, we observed that the $LiPF_6$ salt fully dissolved with stirring after 5 days. Insoluble formulations are depicted by red X's. The complete list of soluble and insoluble formulations with salt concentrations and EMC:VC (w/w) ratios can be found in Table S1. Henceforth, electrolyte compositions are defined by mole fractions and the baseline formulation is 0.1:0.72:0.18 $LiPF_6$:EMC:VC. The solubility range for this electrolyte system is dictated by the salt-to-solvent ratio, where an $LiPF_6$/EMC molar ratio greater than 0.7 resulted in an insoluble formulation. Additionally, the electrolyte composition is not limited by the VC concentration. This suggests that (1) VC is not prominent in the solvation shell of the electrolyte (due to lack of lower solubility limit) and (2) EMC is a major species in the coordination structure. Indeed, this is confirmed by MD simulations and FTIR results discussed later.

We measured the ionic conductivities of the $LiPF_6$:EMC:VC electrolytes to ensure the electrochemical data sets were comparable. These measurements were performed in a dry room environment (−70 °C dew point) at room temperature (25 °C). The ionic conductivities for each electrolyte formulation are shown in Table S1. Shown in Figure 3, the heat map of the ionic conductivities is overlayed with the composition diagram. The ionic conductivity of the baseline 0.1:0.72:0.18 $LiPF_6$:EMC:VC formulation was 7.55 mS cm^{-1}. For the varying $LiPF_6$ molar fraction (x_{LiPF6}) electrolyte composition, we observe that the ionic conductivity rises from 1.04 to 7.55 mS cm^{-1} as x_{LiPF6} increases from 0.01 to 0.10. Subsequently, as the salt content continues to increase from 0.10 to 0.25, the ionic conductivity drops from 7.55 to 3.23 mS cm^{-1}. This unimodal distribution peaks at approximately 0.1 x_{LiPF6} (equivalent to 1.2 M) and has been observed in other nonaqueous electrolytes such as Gen2.[56,57] The maxima is a result of a balance between the ionic carrier number and the ionic mobility. Thus, at low salt concentration

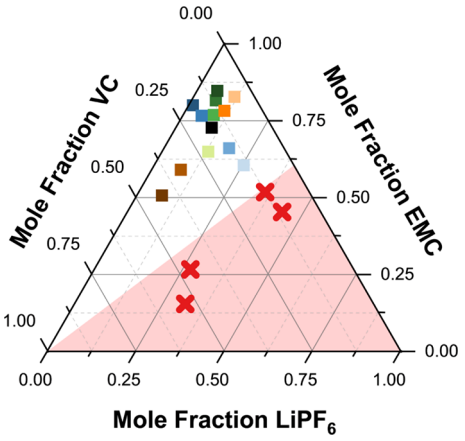


Figure 2. Ternary diagram containing varying soluble $LiPF_6$:EMC:VC formulations as shown by squares. Insoluble electrolyte compositions are depicted by red X's and regions.

(x_{LiPF6} <0.1), charge carrier deficiencies result in lower ionic conductivities.[57,58] At higher concentrations (x_{LiPF6} >0.1), the viscosity and increased fraction of ion pairing limit the ionic conductivities. More specifically, a higher viscosity and prevalence of bulky coordination shells such as AGG lead to lower ion mobility.[58,59] For the varying EMC mole fraction (x_{EMC}) formulations, as x_{EMC} increases from 0.64 to 0.84, the ionic conductivity drops from 7.95 to 3.42 mS cm^{-1}, likely due to the decreased concentration of ionic carriers. Interestingly, we observed an ionic conductivity rise from 5.97 to 10.00 mS cm^{-1} as the VC mole fraction (x_{VC}) increases from 0.06 to 0.42. These results align with AEM-derived ionic conductivities that span from 0.2 to 10.2 mS cm^{-1} in Figure S1. Overall, the narrow formulation-dependent ionic conductivity ranged from 1.04 to 10.00 mS cm^{-1}, allowing for comparison of calendar aging results that are not biased by poor ion transport; varying current relaxation kinetics could affect the interpretation of voltage hold data for silicon.[23]

Calendar aging experiments with each electrolyte composition were done to quantify the averages (solid lines) and standard deviations (bands). The fitted parameters (Q_{nom}, Q_{hold}, Q_{rev}, a, c, and p, from eqs 1 and 2), cumulative hold (Q_{hold}^{final}), reversible capacity (Q_{rev}^{final}), and irreversible capacity (Q_{irrev}^{final}) can be found in Figures S2 and S3. The estimated calendar lifetime profiles for $LiPF_6$ and VC varying formulations are shown in Figure S4 while Table S2 contains normalized calendar lifetime at 80% capacity for all formulations. With the residual current profile measured via the 500 h V-hold protocol, we extracted the estimated calendar lifetimes (Figure 4a) and depicted the calendar lifetime at 80% relative capacity in a contour diagram with the electrolyte compositions overlayed (Figure 4b). The calendar lifetimes are normalized to the time at which the capacity exchanged by the baseline formulation (0.1:0.72:0.18 $LiPF_6$:EMC:VC) during the V-hold equals 80% of the nominal cell capacity (t = 244 h).

The normalized calendar lifetimes (Figure 4b) reveal higher EMC concentrations (x_{EMC} = 0.72 → 0.84) lead to lower calendar lifetimes (1.0 → 0.25 relative estimated calendar lifetime), but decreasing the EMC content from the baseline formulation does not impact aging performance. Indeed, Student t test p values indicate that raising the EMC content above the baseline formulation has a statistically significant

Downloaded from pubs.acs.org/aamick/article-pdf/18/38/52238/6858305O/am-2025-23255a.pdf by LAWRENCE BERKELEY NATL LABORATORY user on 06 November 2026

https://doi.org/10.1021/acsami.5c23255
ACS Appl. Mater. Interfaces 2026, 18, 52238−52252

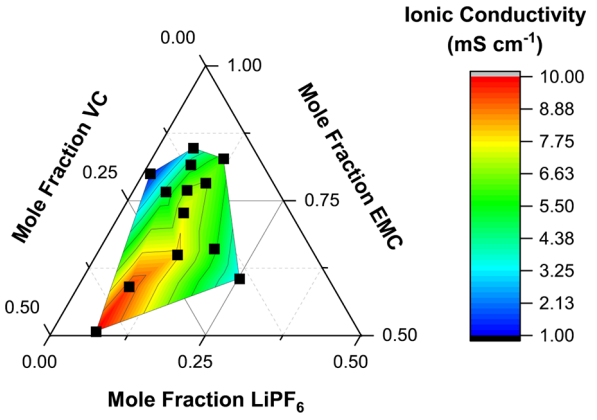


Figure 3. Heat map of ionic conductivities with varying $LiPF_6$:EMC:VC formulations represented as black squares. Ionic conductivity measurements were performed in a dry room at room temperature.

effect (p value <0.05) on the surface passivity while the 0.64 and 0.72 x_{EMC} compositions possess a p value of 0.843 (Table S3). Contrary to the negative correlation between EMC and calendar lifetime, VC shows a positive trend with surface passivity, where decreasing the VC content from 0.17 to 0.11 mole fraction causes the calendar lifetime to drop by 98%. Moreover, formulations with higher x_{VC} than 0.17 exhibit relative estimated calendar lifetimes that range from 1 to 1.04, showing no change in the aging performance (Table S3). The relation between aging and VC indicates that while VC is essential for surface passivation for this electrolyte system, increasing the VC content yields diminishing returns on calendar life improvements. Interestingly, we observe no significant changes in the calendar aging performance as a function of the salt content (Figure 4b). As the $LiPF_6$ concentration rises from 0.01 to 0.25 mole fraction, the estimated calendar lifetime ranges between 0.63 and 1.01. We note that although the 0.05 $xLiPF_6$ formulation exhibited an estimated calendar lifetime of 0.63, the calculated p values show no statistical significance (Table S3).

To explore the solvation structure shifts as a function of the electrolyte formulation, we performed MD simulations on varying $LiPF_6$:EMC:VC formulation systems in triplicates to ascertain the fraction of SSIP, CIP, and AGG solvation structures. For the baseline formulation, the coordination structure populations are 59.5%, 38.0%, and 2.5% for the SSIPs, CIPs, and AGGs, respectively (Figure 5a–c). These populations shift with electrolyte composition. Increasing x_{LiPF6} from 0.01 to 0.25 led to the following shifts: SSIP (69.4% → 11.0%), CIP (30.3% → 47.2%), and AGG (0.3% → 41.7%). The higher AGG fraction (Figure 5c) decreases the bulk ion transport, which matches the lower experimental ionic conductivities measured at high-salt concentrations. Additionally, the lower ionic conductivities could also stem from the switch from an SSIP to CIP-dominated population. CIPs possess sluggish ionic mobility due to charge balance whereas the dipole moment caused by solvent separation of the anion and Li^+ boosts transport kinetics.[60,61] Interestingly, varying the EMC content does not shift the overall coordination environments in the electrolyte where the fractions of SSIP (55.5–60.2%), CIP (37.9–42.7%), and AGGs (1.7%–3.9%) do not drastically change. This is attributed to the dominance of EMC as the highest concentration speciate in any of the soluble electrolyte formulations within the inner solvation sheath, which we will discuss in a later section. For the varying VC formulations, the SSIP (51.4% → 77.5%) and CIP (45.3% → 21.6%) fractions shift, while the AGG (3.9% → 0.9%) populations remain comparatively constant as x_{VC} increases from 0.05 to 0.42. This agrees with the conductivity results where raising the VC content of the electrolytes forms an SSIP-rich electrolyte while decreasing the CIP and AGG fractions, thereby improving ion mobility.

In addition to the solvation structures, we obtained the coordination numbers for PF_6^-, EMC, and VC via MD simulations in triplicates. Average coordination numbers with standard errors are shown in Table S4. Unlike spectral data, the solvation numbers (N) extracted from the MD simulations in this work include only species that directly interact with the Li^+ and therefore ignore the secondary and outer solvation shells. These exchange dynamics result in higher experimental N_{EMC} than simulated values. As shown in Figure 6a, increasing the $LiPF_6$ (0.01 → 0.25) and VC (0.06 → 0.42) mole fractions shift N_{EMC} from 3.43 to 2.34 and from 3.56 to 3.01, respectively. Contrarily, a positive correlation exists between x_{EMC} (0.64 → 0.84) and N_{EMC} (3.24 → 3.54). Illustrated in Figure 6b,c, both N_{PF6-} and N_{VC} range from 0.24 to 1.30 and increase with their respective constituent concentrations. Although the electrolyte formulations mainly consist of EMC, by dividing N_{VC} and N_{EMC} by their respective component mole fractions for the 0.72:0.18 and 0.51:0.42 EMC:VC formulations, we find the normalized coordination ratio for both compositions is 2.1:1 (normalized N_{EMC}/N_{VC}). This indicates that the higher EMC coordination relative to VC is not solely due to the high EMC content. Interestingly, we observe that N_{EMC} correlates with the calendar lifetime, where increasing the solvent coordination from 2.34 to 3.56 results in a 98% lower calendar lifetime (Figure 4b). Indeed, as depicted in Figure 6d, the normalized calendar lifetime remains constant (1–1.04) at N_{EMC} <3.4. Above N_{EMC} = 3.4, the normalized calendar lifetime begins to drop from 1 (N_{EMC} = 3.4) to 0.02 (N_{EMC} = 3.56) indicating that the presence of EMC within the first solvation sheath plays a detrimental role in Si surface passivity. In Figure S5, the aging performance stochastically trends with the anion and VC coordination numbers indicating that these solvated species exert lower influence on the normalized calendar lifetime compared to EMC. We note that although charge scaling shifts the calendar lifetime drop threshold (Figure S6), elevated solvent coordination still correlates with lower calendar aging performance. Additionally, the MD simulation results were experimentally verified with attenuated total reflectance Fourier transform infrared spectroscopy (Figures S7 and S8). Nevertheless, to probe the aging threshold phenomenon, we investigated the SEI chemical composition as a function of the electrolyte formulation, which plays a role in the SEI–electrolyte interactions that occur during aging.

The post-formation cycle SEI surface composition was probed via XPS as a function of the electrolyte composition. We note that electrodes were rinsed with DMC to remove residual salt that would result in spectral artifacts that arise from salt photodegradation but may dissolve portions of the SEI.[5,62,63] Low atomic percentages (at % <5%) of P2p species (Figure S9) indicate successful residual salt removal. Additionally, the lack of Si signals suggests that the SEI is thicker than 10 nm. From the fitted C 1s spectra (Figure 7a), the insoluble carbon species comprise Li_2CO_3 (290.0 eV),

Downloaded from pubs.acs.org/aamick/article-pdf/18/38/52238/6858050/am-2025-23255a.pdf by LAWRENCE BERKELEY NATL LABORATORY user on 06 November 2026

https://doi.org/10.1021/acsami.5c23255
ACS Appl. Mater. Interfaces 2026, 18, 52238–52252

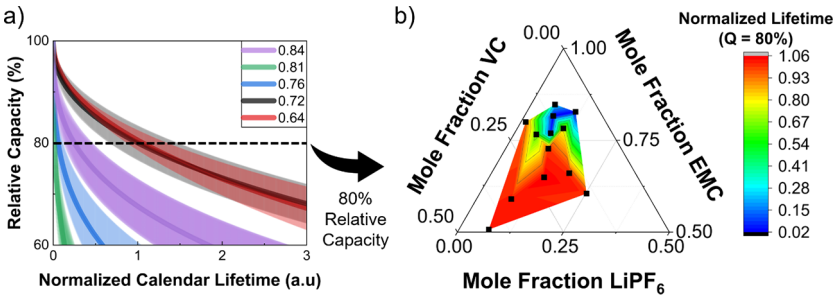


Figure 4. (a) Estimated normalized calendar lifetime profiles for varying x_{EMC} electrolyte formulations. The calendar lifetimes are normalized to 0.10:0.72:0.18 $LiPF_6$:EMC:VC baseline formulation. The calendar lifetime averages and standard deviations are obtained from triplicate V-hold tests and are denoted as solid lines and bands, respectively. (b) The average normalized calendar lifetime for each electrolyte composition at 80% relative capacity was extracted and is depicted as a contour map with the compositional diagram overlaid.

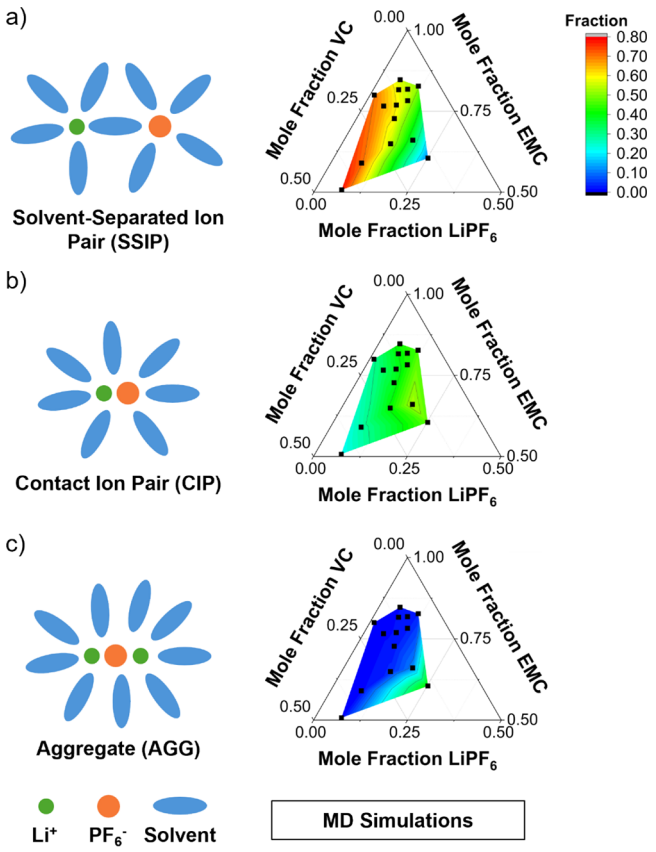


Figure 5. Heat maps of solvation structure ratios as defined by the inner solvation shell for (a) solvent-separated ion pairs, (b) contact ion pairs, and (c) aggregates. These fractions are extracted via MD simulations of varying $LiPF_6$:EMC:VC electrolyte compositions.

C−O (286.5 eV), and alkanes (284.8 eV).[5] The alkane species coincide with the total organic content within the electrolyte where, at higher EMC and VC mole fractions, the C−C at % increases from 10.7 to 21.5 (Figure 7b). Intuitively, the alkane content stems from the VC and EMC due to the lack of carbon in $LiPF_6$. On the other hand, increasing x_{LiPF6} from 0.01 to 0.25 shifts the C−O SEI species from 1.0 to 10.5 at % (Figure 7c). Depicted in Figure 7d, increasing $xLiPF_6$ from 0.01 to 0.25 diminishes the Li_2CO_3 at % from 11.7 to 2.6. Because the amount of Li_2CO_3 does not significantly change with EMC and VC concentrations, $LiPF_6$ likely plays a mechanistic role in the formation of Li_2CO_3. The C 1s XPS spectra results align with the fits obtained from the O 1s spectra (Figure S10).

In F 1s spectra (Figure 8a), the estimated fluorine amount (Figure S9) ranges from 0.2 to 14.5 at % and consists of LiF (685.0 eV) and $Li_xPO_yF_z$ (687.5 eV).[64,65] Increasing $xLiPF_6$ from 0.01 to 0.25 raises the LiF (0.1 to 6.84 at %) and $Li_xPO_yF_z$ (0.1 to 7.7 at %) content (Figure 8b,c) indicating that these SEI species are from $LiPF_6$ decomposition during formation cycling. The absolute concentrations of fluorinated species remain relatively low (at % <5) and the SEI is dominated by carbon-containing products. This indicates that decomposition of EMC and VC contributes more extensively to SEI formation under these conditions, while $LiPF_6$ decomposition leads to the formation of fluorinated species in smaller amounts. To provide further evidence, the LiF, $Li_xPO_yF_z$, and Li_2CO_3 atomic percentages as a function of salt concentration as well as the EMC, VC, and PF_6^- coordination numbers are depicted in Figure 9a,b. As the concentration increases (0.12–3.50 M), the LiF, $Li_xPO_yF_z$, and N_{PF6-} grows proportionally while both Li_2CO_3 and N_{EMC} exhibit an inverse relationship with $LiPF_6$ concentration. We note that although N_{VC} shows no relation with concentration, other studies have shown the production of Li_2CO_3 and polymeric species from the ring-opening reaction of VC.[32,66,67] Overall, higher EMC and VC content favors the formation of alkanes, C−O species, and Li_2CO_3, whereas increasing $LiPF_6$ concentration promotes the formation of LiF and $Li_xPO_yF_z$, which matches with other works.[68−70] Additionally, even at high salt concentration (3.5 M), the $LiPF_6$:EMC:VC electrolyte produces an organic-rich SEI with less than 15.0 at % fluorine species. These positive correlations between the coordination numbers and SEI components suggest that the initial SEI composition can be tuned via the inner solvation sheath for this electrolyte system.

To elucidate the aging effects on SEI surface composition (Figure 10), we performed XPS on the Si electrodes post-V-hold protocol. Like the post-formation compositional analysis, a DMC rinse was used to remove residual salt with the tradeoff of possible SEI removal. The lack of Si signal indicates that the SEI continues to be thicker than 10 nm even after aging. The difference between the post-aged and post-formation was calculated. This difference is denoted by Δat % where positive and negative values indicate a growth and decline, respectively, of a species after aging. The elemental composition contour diagrams for the fitted XPS spectra post-V-hold protocol are shown in Figure S9. After the 500 h V-hold procedure, the

Downloaded from pubs.acs.org/aamick/article-pdf/18/38/52238/6858305O/am-2025-23255a.pdf by LAWRENCE BERKELEY NATL LABORATORY user on 06 November 2026

https://doi.org/10.1021/acsami.5c23255
ACS Appl. Mater. Interfaces 2026, 18, 52238−52252

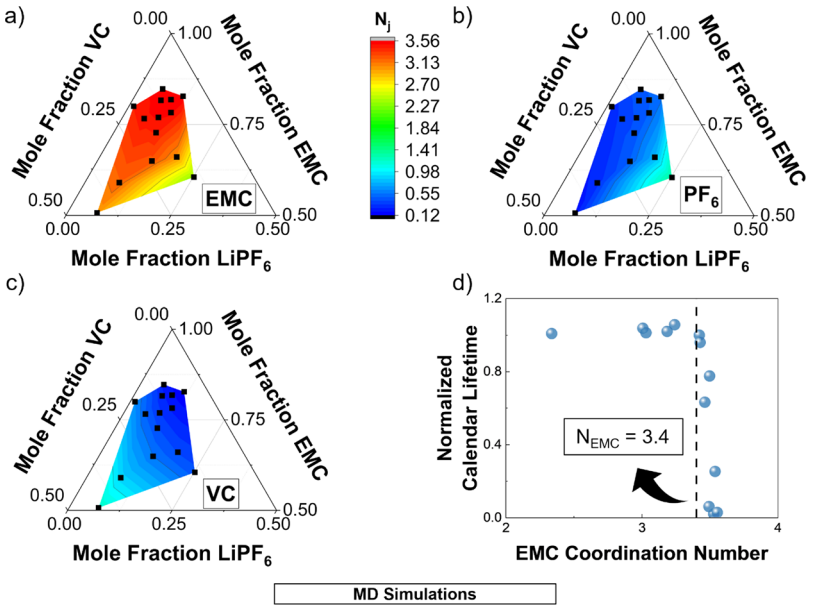


Figure 6. Heat maps of simulated (a) EMC, (b) PF_6, and (c) VC solvation numbers obtained via MD calculations found overlayed onto the electrolyte composition map. The (d) normalized calendar lifetime obtained from V-hold tests is displayed as a function of the EMC coordination number. The dotted line represents an EMC coordination number of 3.4 where the normalized calendar lifetime begins to drop.

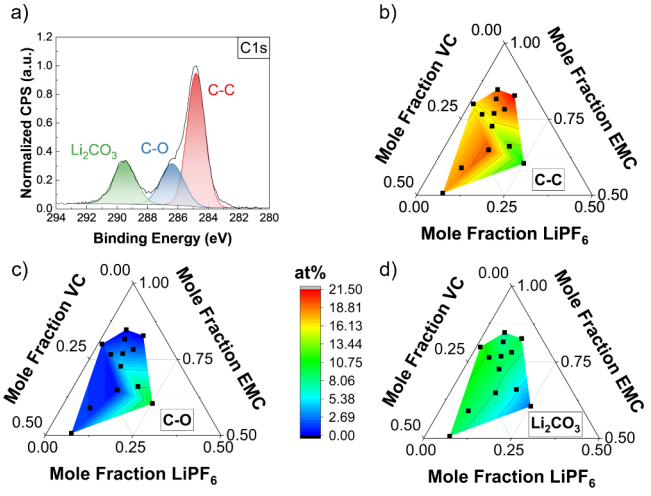


Figure 7. (a) Example C 1s spectrum for a post-formation cycling electrode using 0.06:0.84:0.10 $LiPF_6$:EMC:VC electrolyte formulation. By fitting the C 1s spectra, the (b) C−C, (c) C−O, and (d) Li_2CO_3 heat maps were extracted with the electrolyte composition diagram overlayed (black dots).

changes in the elemental composition are most prevalent in the Li1s and C 1s species, where each span between −17.5 to −7.9 and −3.2 to 15.3 Δat %, respectively, indicating diminished Li and increased C content within the SEI after aging. The overall Δat % of oxygen (−8.5 to 3.8), fluorine (−2.6 to 5.1), and phosphorus (−0.1 to 3.1) shows no significant changes (Δat % <5) after aging. These observed changes are attributed to shifts in organolithium species at % due to the decreased surface lithium content and somewhat constant phosphorus and fluorine levels. For example, the baseline formulation exhibits Li and C Δat % of −11.4% and 12.1%, respectively. To explore this notion further, we examined the C 1s spectra and the associated fits.

The shifts in the carbon elemental composition primarily manifest in changes of the C−O SEI moieties post-aging (Figure 11). Indeed, the change in surface C−O species is inversely proportional to the salt content, where decreasing $xLiPF_6$ from 0.25 to 0.01 results in the C−O Δat % increasing from −1.3 to 16.8 at %. The contour maps for the C 1s XPS fits of post-aged Si electrodes are depicted in Figure S11. Although a substantial change in C−O content (∼8.0 Δat %) is present with different EMC and VC formulations, we observe no trend with changing the electrolyte composition of these components, where the C−O Δat % ranges from 5.7 to 9.4 Δat %. The shifts in C−O Δat % suggest solvent decomposition during calendar aging. Furthermore, the observed trend between salt concentration and C−O Δat % indicates that the magnitude of decomposition is dictated by the initial total organic content within the electrolyte. On the other hand, the Δat % of alkane and Li_2CO_3 species vary between −2.9 and 8.5 and between −2.1 and 1.2, respectively, indicating little change in these SEI species post-aging. In addition to Li_2CO_3, the Δat % of other inorganic SEI components, namely, LiF and $Li_xPO_yF_z$, remain constant after calendar aging as presented in Figure 12. Contour maps for the post-aged XPS F 1s are shown in Figure S12. We surmise that the organolithium SEI components undergo dissolution and are replaced by C−O species derived from electrolyte decomposition during calendar aging. Although the C−O Δat % does not trend exactly with the calendar lifetime data, the magnitude of the SEI compositional shift suggests a role in the Si surface passivity during aging.

AEM was performed to further support the notion of SEI dissolution and subsequent electrolyte decomposition. We note that a larger electrolyte composition range was utilized for AEM compared to the experimental electrolyte formulations. In Figure 13a, the dielectric constant of the electrolyte ranges from 8.2 to 50.0 and is formulation dependent. Extended discussion of this formulation-dependent behavior can be found in the Supporting Information. Within the experimental

https://doi.org/10.1021/acsami.5c23255
ACS Appl. Mater. Interfaces 2026, 18, 52238−52252

Downloaded from pubs.acs.org/aamick/article-pdf/18/38/52238/6858305O/am-2025-23255a.pdf by LAWRENCE BERKELEY NATL LABORATORY user on 06 November 2026

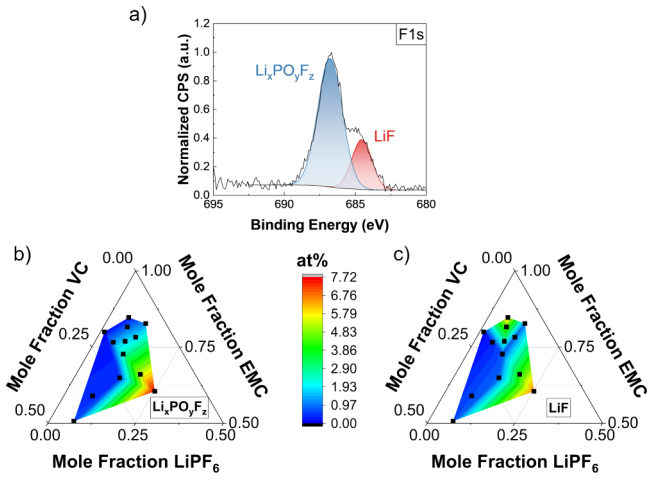


Figure 8. (a) Example of F 1s spectrum of post-formation Si electrode using 0.06:0.84:0.10 $LiPF_6$:EMC:VC electrolyte. Contour maps of the (b) $Li_xPO_yF_z$ and (c) LiF content are derived from the fits.

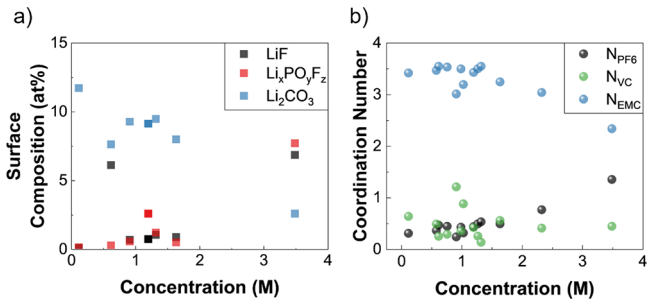


Figure 9. (a) LiF, $Li_xPO_yF_z$, and Li_2CO_3 at % (squares) obtained from XPS fitting of Si electrodes post-formation cycling and (b) coordination numbers (spheres) of PF_6^-, VC, and EMC from MD simulations as a function of electrolyte salt concentration.

composition range, a comparison between the calendar aging performance (Figure 4) and relative dielectric constant indicates that the calendar lifetime is constant (~1) with ε above 18.4. Below ε = 18.4, the Si surface passivity begins to suffer where the electrolyte dielectric constant reaches 14.7 at a calendar lifetime of 0.25 (0.06:0.84:0.10 $LiPF_6$:EMC:VC). This suggests that the electrolyte's dielectric constant plays a role in the anode interfacial stability, and a low ε could lead to the dissolution of low-polarity SEI species (e.g., organolithium).

As shown in Figure 13b, we calculated the total free solvent fraction as a function of the electrolyte composition to investigate the participation of free solvents in continuous electrolyte decomposition during calendar aging. Total free solvent fraction is defined as the mole fraction of solvent that is non-associated (but may be self-associating). Intuitively, the total free solvent fraction exhibits an inverse relationship with the $LiPF_6$ concentration, where increasing x$LiPF_6$ from 0.01 to 0.25 results in a free solvent fraction drop from 0.96 to 0.28. The total free solvent fraction trends well with the change in carbon content before and after aging (Figure 10) suggesting non-coordinated solvents are involved in electrolyte decomposition during aging. The relationship between C−O Δat % and total free solvent fraction in a scatter plot can be found in Figure S13a,b. Contour maps of the calculated free solvent fractions of EMC

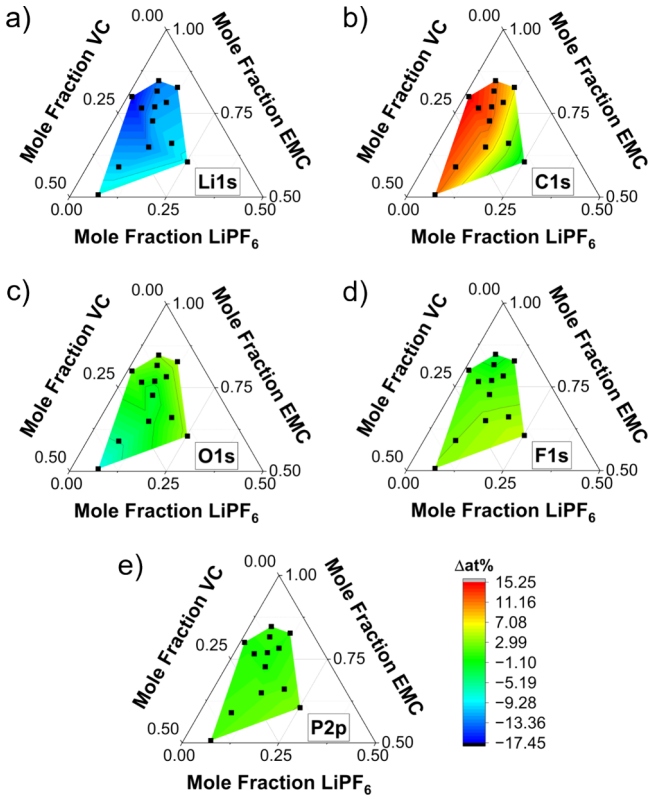


Figure 10. $LiPF_6$:EMC:VC electrolyte formulation ternary diagram with contour maps of (a) Li1s, (b) C 1s, (c) O 1s, (d) F 1s, and (e) P2p at % changes before and after the 500 h V-hold protocol. Δat % represents the difference between the SEI composition after the 500 h V-hold protocol and formation cycling.

and VC are shown in Figure 13c,d. The EMC free solvent fraction (0.03 to 0.26) is comparatively lower than the VC free solvent fraction (0.25 to 0.75) within the experimental electrolyte formulation range. This aligns with the higher N_{EMC} relative to N_{VC} derived from MD simulations previously discussed. Although we cannot completely deconvolute the decomposition of the free solvents, the larger free VC fraction along with its agreement with the C−O Δat % suggests the preferential decomposition of free VC over EMC during aging (Figure S13b).

In this work, we systematically varied $LiPF_6$:EMC:VC formulations to find the relationship among solvation structure, SEI composition, and calendar aging performance. The following paragraphs will revolve around comparison of the VC-based electrolyte to other electrolyte systems as well as aging mechanism discussions. The 0.1:0.72:0.18 $LiPF_6$:EMC:VC baseline formulation exhibited an average Q_{irrev} of 27.1%. In comparison to a previous calendar aging study performed by Verma et al. on the Gen2 and Gen2F electrolytes, the loss of lithium inventory during calendar aging ranks as follows: Gen2 > $LiPF_6$:EMC:VC ≈ Gen2F.[24] However, we note that the V-hold protocols between studies were not consistent and do not allow for quantitative comparisons. Interestingly, the Gen2F and LiPF:EMC:VC electrolytes exhibit similar calendar aging performances. This might be due to the reduction of FEC to form VC in the Gen2F electrolyte, as shown by Michan et al.[37] For the Gen2 electrolyte, Malkowski et al. revealed that EC and $LiPF_6$ increased the parasitic currents

https://doi.org/10.1021/acsami.5c23255
ACS Appl. Mater. Interfaces 2026, 18, 52238−52252

Downloaded from pubs.acs.org/aamick/article-pdf/18/38/52238/6858305O/am-2025-23255a.pdf by LAWRENCE BERKELEY NATL LABORATORY user on 06 November 2026

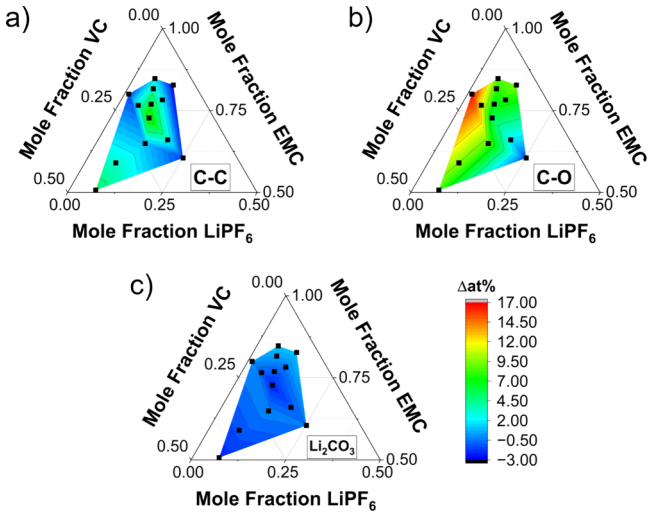


Figure 11. Heat maps of changes in at % before and after the 500 h V-hold protocol for (a) C−C, (b) C−O, and (c) Li_2CO_3 are derived from the XPS C 1s fits. Δat % represents the difference between the SEI composition after the 500 h V-hold protocol and formation cycling.

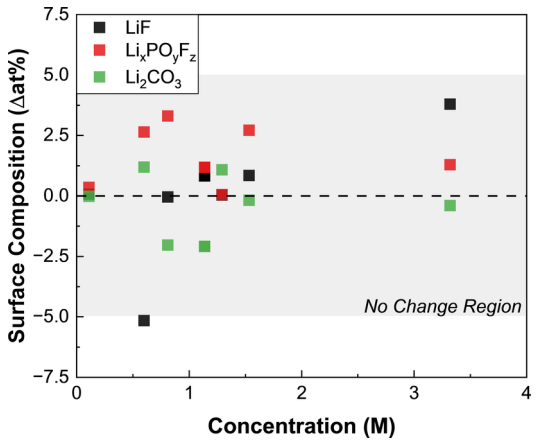


Figure 12. Atomic percentage changes post-aging in LiF (black squares), $Li_xPO_yF_z$ (red triangles), and Li_2CO_3 (green circles). Δat % is the difference between the SEI composition after the 500 h V-hold protocol and formation cycling. The gray region represents post-age Δat % that is within XPS instrumental analysis parameters (~5.0%) and indicates no species concentration change.

associated with insufficient surface passivity during calendar aging, whereas EMC acted as a spectator.[25] This contrasts with the $LiPF_6$:EMC:VC electrolyte, where the calendar aging is mainly a function of EMC and VC content, and the $LiPF_6$ does not play a significant role in surface passivity. Furthermore, the enhancement of calendar life with increasing VC content ($LiPF_6$:EMC:VC) contrasts with the negative impact of EC (Gen2) in aging performance, which shows differences in surface passivation between the two carbonates. However, much like the Gen2 electrolyte, the VC-based system showed no trend between initial SEI composition and loss of lithium inventory while also containing roughly half of the LiF at %.

The solvation structure differences between the Gen2 and VC-based electrolyte may explain the variations in calendar

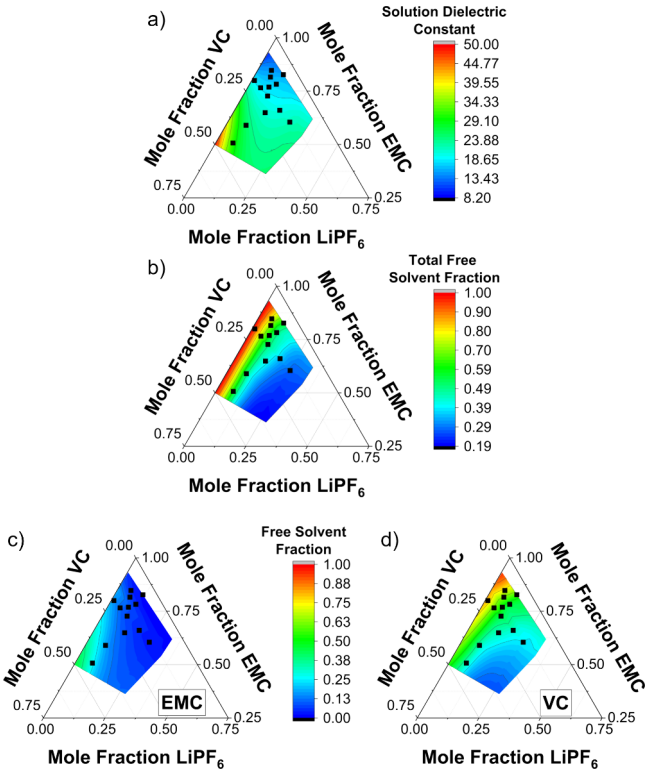


Figure 13. AEM-derived contour maps for (a) dielectric constant, (b) total free solvent fraction, (c) free EMC fraction, and (d) free VC fraction at 20 °C. Total free solvent fraction is defined as the mol fraction of solvent that is non-coordinated. Note: a larger span of electrolyte formulations was explored with the simulation. The experimental electrolyte compositions are denoted by black squares.

aging performance. Through MD simulations, Hou et al. found the Gen2 electrolyte to contain equivalent fractions of SSIP (35.6%), CIP (33.3%), and AGG (31.1%) coordination structures.[31] Additionally, the N_{EC} and N_{EMC} for the SSIP structures were 1.8 and 2.3, respectively, whereas the CIP and AGG possessed N_{EMC} of 3 and N_{EC}/N_{PF6-} near 1. The $LiPF_6$:EMC:VC electrolyte in this work possesses higher SSIP fraction (~59.5%), which manifests in the low N_{PF6-} (0.43). When compared to the Gen2 electrolyte, the lack of trend between the salt concentration and calendar aging performance for the VC-based electrolyte suggests the lower Li^+-anion interaction leads to improved surface passivation. The contradicting trends between EMC and calendar life between the two electrolyte systems indicate mechanistic differences in calendar aging. More specifically, due to the plateauing improvement of aging performance with the increasing VC content and EMC-dominant coordination shell of the VC-based electrolyte (N_{EMC} = 3.4, N_{total} = 4.3), the EMC–SEI interactions may dictate the Si surface passivity. This is reflected in the calendar aging data (Figure 4). For the Gen2 system, EMC may act as a spectator due to the overarching detrimental impact of EC and $LiPF_6$ on the surface passivation.

From our previous work, we revealed the calendar aging performance of LiFSI:TMS:TTE to be independent of the LHCE formulation and initial SEI composition.[71] Additionally, due to the weak Li^+-TMS interaction, the solvation structure remained constant as a function of LHCE formulation. When comparing LHCE to the VC-based electrolyte in this study, the LHCE

https://doi.org/10.1021/acsami.5c23255
ACS Appl. Mater. Interfaces 2026, 18, 52238−52252

Downloaded from pubs.acs.org/aamick/article-pdf/18/38/52238/6858050/am-2025-23255a.pdf by LAWRENCE BERKELEY NATL LABORATORY user on 06 November 2026

demonstrates superior passivating ability. However, much like previous aging studies, we cannot quantitatively compare the calendar aging performances between the two electrolyte systems due to V-hold protocol differences. Nevertheless, the contrasting observations in formulation-dependent solvation structure changes in the two electrolytes may be the underlying cause of the $LiPF_6$:EMC:VC electrolyte's worse passivating ability. Interestingly, although the electrolytes' LiF content is approximately equivalent to the baseline compositions, the discrepancies in calendar lifetime suggest that simply achieving a LiF-rich SEI may not be an effective strategy in improving Si surface passivity. These discrepancies could be attributed to the SEI–electrolyte interactions that occur during aging such as HF attack and SEI dissolution.

HF attack has been identified as a possible calendar aging mechanism within Si-based anodes.[2,4] Unlike the LiFSI in the LHCE, the Gen2 and VC-based electrolytes contain $LiPF_6$, which is most susceptible to the hydrolysis reaction.[72] From Karl-Fischer titration, the measured water content for each electrolyte formulation ranged from 23.4 to 52.7 ppm water, indicating the success of the drying procedure. We note that attempted water content measurements of pure EMC and VC failed. This suggests both solvents possess a water content below the titrator's detectable limit (<1 ppm water). For the small amount of residual water left in the electrolyte, VC may function as a sacrificial water scavenger, thereby preventing $LiPF_6$ hydrolysis. This could occur during the initial conditioning cycles before calendar aging. Indeed, Gogoi et al. revealed through NMR and FTIR that VC undergoes a ring-opening reaction to form polymeric species and CO_2 in the presence of water.[67] Calendar lifetime improvements with the addition of VC up to the baseline formulation may stem from the water scavenging ability of the cyclic carbonate. The diminishing returns on surface passivity improvements indicate that the baseline 0.18 x_{VC} contains sufficient VC to scavenge water impurities. Indeed, AEM revealed the presence of free VC that would be available for hydrolysis. Hence, an alternative mechanism to HF attack is likely contributing to the VC-based electrolyte's composition-dependent performance.

SEI dissolution could explain the shifts in calendar lifetime and solvation structure as a function of electrolyte formulation.[73] This is consistent with the previously mentioned electrochemical quartz crystal microbalance mass loss measurement study.[18] The SEI dissolution mass loss increased from approximately 7% to 60% with lower LiFSI salt concentrations in a 1,2 dimethoxyethane (DME) electrolyte (4 to 0.5 M). Such results match the trends between the salt concentration and SEI species Δat % observed in this species, further evidencing SEI dissolution as a primary degradation mechanism. Solid-phase conversion could occur within the SEI during aging and would likely manifest in Li_2CO_3 decomposition to lithium oxide (Li_2O), which has been extensively studied.[74,75] However, the lack of Li_2O in the O 1s XPS spectra (Figure S10e) at 529.5 eV indicates that solid-phase conversion is unlikely.[19,76,77] From MD simulations, the $LiPF_6$:EMC:VC electrolyte's surface passivation trends with N_{EMC} as well as the AEM-derived dielectric constant where ε <18.4 is detrimental to the calendar lifetime. A consequence of lower-dielectric EMC-rich systems is the greater fraction of ion-associated species, which are less solvated than their free (non-ion-associated) counterparts, allowing a greater population of free solvent to either react at the surface (VC) or promote SEI dissolution (EMC). The organic SEI species would be more likely to dissolve than their inorganic analogs, given EMC's low dielectric constant ($\varepsilon \approx 2.98$).[78] While the C−O and lithium content Δat % do not perfectly coincide with the calendar lifetime, a significant shift in SEI composition post-aging and trend between performance and N_{EMC} still indicates that dissolution of the surface film occurs. Thus, the loss of organolithium species after aging is attributed to SEI dissolution via EMC in the VC-based electrolyte. As the Si anode continues to age, SEI dissolution would expose Si surfaces, resulting in continuous electrolyte degradation that we observed in the increased C−O Δat %. For noncoordinated species, AEM results allude to the preferential decomposition of VC over EMC. The plateauing behavior observed between the VC content and the aging performance, which suggests sufficient VC, must be present to rebuild the SEI and improve the normalized calendar lifetime. We note that for noncoordinating VC to reduce, given its reduction potential (~1.2 V vs Li/Li^+), a substantial potential drop across the SEI must be present.[79] However, further investigation of this phenomenon warrants a separate study. Nevertheless, constant electrolyte decomposition would eventually lead to electrolyte depletion that would be detrimental to calendar aging. In summary, the data suggests that the EMC-rich solvation structure of the $LiPF_6$:EMC:VC electrolyte leads to SEI dissolution and reconstruction via continuous electrolyte decomposition during calendar aging. This may be the key mechanism behind calendar aging differences between the LHCE and prototypical electrolyte systems.

CONCLUSIONS

In this study, we deconvoluted the roles of the electrolyte constituents in a $LiPF_6$:EMC:VC electrolyte by extracting the estimated calendar lifetimes from the residual current profiles obtained during V-hold aging in 13 different electrolyte formulations. The estimated calendar lifetimes were then related to the SEI composition, ionic conductivity, and coordination structure changes as a function of electrolyte formulation. The key findings are as follows:

- EMC content rising from 0.64 to 0.84 moles leads to a drop-in normalized calendar lifetime from 1.06 to 0.25. This trends well with N_{EMC} obtained via MD simulations where increasing N_{EMC} lowers the Si surface passivity. The EMC-rich solvation shell may lead to SEI dissolution where the low dielectric strength of EMC ($\varepsilon = \sim 3$) may dissolve the low-polar SEI components during calendar aging.
- We observe that the addition of VC is crucial to improving the calendar lifetime of the $LiPF_6$:EMC:VC electrolyte. Increasing the VC content from 0.11 to 0.18 mole fraction improves the calendar lifetime from 0.02 to 1. However, further raising x_{VC} above 0.18 does not yield significant calendar lifetime improvements. This suggests that an excess of VC does not decrease the rate of SEI growth and parasitic reactions. However, a higher VC content could still prolong calendar life for as long as sufficient VC remains available to act as a sacrificial agent. Furthermore, AEM showed an abundance of free VC (0.25–0.75 mole fraction of free solvent). A portion of the free VC could scavenge trace water impurities within the electrolyte, forming polymeric products that precipitate onto the electrode surface,

Downloaded from pubs.acs.org/aamick/article-pdf/18/38/52238/6858305O/am-2025-23255a.pdf by LAWRENCE BERKELEY NATL LABORATORY user on 06 November 2026

https://doi.org/10.1021/acsami.5c23255
ACS Appl. Mater. Interfaces 2026, 18, 52238−52252

and prevent possible water-induced calendar life degradation.

- Increasing x_{LiPF6} from 0.01 to 0.25 results in no significant change in the estimated calendar lifetime indicating that the anion does not play a significant role in the aging performance.
- Post-aging XPS analysis reveals a drop in Li content by 17.5 to 7.9 Δat % while the C content increases by up to −3.2 to 15.3 Δat %. All other elements remain constant. The C content shift stems from changes in the C−O species (−1.3 to 16.8 Δat %) and trends with the free VC fraction within the electrolyte. This SEI compositional shift suggests that organolithium species undergo dissolution and are replaced by organic C−O rich species—possibly from VC decomposition. Although the C−O Δat % does not trend exactly with the calendar life performance, the continuous electrolyte consumption would lead to electrolyte depletion and capacity fade.

The aging performance differences between the Gen2 and the VC-based electrolyte may be due to the comparatively higher Li^+–solvent interactions within the latter electrolyte system. Compared to the LiFSI:TMS:TTE LHCE, the $LiPF_6$:EMC:VC electrolyte exhibits worse calendar life, which we attribute to the EMC-rich solvation structure and formulation-dependent solution dielectric constant that promotes SEI dissolution and reconstruction, leading to worse Si surface passivity. Overall, we believe that these findings provide crucial insight into the roles of electrolyte components in the calendar aging mechanisms of Si anodes.

■ ASSOCIATED CONTENT

Supporting Information

The Supporting Information is available free of charge at https://pubs.acs.org/doi/10.1021/acsami.5c23255.

Electrolyte compositional table with water content and ionic conductivities; discussion of Karl-Fischer titration and dielectric constant; Student *t* test values; AEM-derived ionic conductivity heat map; fit parameters from V-hold protocol fitting; MD simulation discussion; ATR-FTIR results and discussion; XPS data (DOCX)

■ AUTHOR INFORMATION

Corresponding Author

Gabriel M. Veith – *Chemical Sciences Division, Oak Ridge National Laboratory, Oak Ridge, Tennessee 37831, United States; Department of Chemical and Biomolecular Engineering, The University of Tennessee Knoxville, Knoxville, Tennessee 37996, United States;* orcid.org/0000-0002-5186-4461; Email: gveith@utk.edu

Authors

Steven Lam – *Chemical Sciences Division, Oak Ridge National Laboratory, Oak Ridge, Tennessee 37831, United States; Department of Chemical and Biomolecular Engineering, The University of Tennessee Knoxville, Knoxville, Tennessee 37996, United States;* orcid.org/0000-0001-5642-9939

Nessa Majaya – *Department of Materials Science and Engineering, University of California Berkeley, Berkeley, California 94720, United States; Materials Science Division, Lawrence Berkeley National Laboratory, Berkeley, California 94720, United States*

Kevin L. Gering – *Idaho National Laboratory (INL), P.O. Box 1625, Idaho Falls, Idaho 83415-3570, United States*

Robert L. Sacci – *Chemical Sciences Division, Oak Ridge National Laboratory, Oak Ridge, Tennessee 37831, United States;* orcid.org/0000-0002-0073-5221

Lydia Meyer – *Energy Conversion and Storage Systems Center, National Laboratory of the Rockies, Golden, Colorado 80401, United States*

Ankit Verma – *Energy Conversion and Storage Systems Center, National Laboratory of the Rockies, Golden, Colorado 80401, United States;* orcid.org/0000-0002-7610-8574

Maxwell C. Schulze – *Energy Conversion and Storage Systems Center, National Laboratory of the Rockies, Golden, Colorado 80401, United States;* orcid.org/0000-0001-8368-4054

Lily A. Robertson – *Chemical Sciences and Engineering Division, Argonne National Laboratory, Lemont, Illinois 60439, United States;* orcid.org/0000-0002-8784-0568

Zhengcheng Zhang – *Chemical Sciences and Engineering Division, Argonne National Laboratory, Lemont, Illinois 60439, United States;* orcid.org/0000-0002-0467-5801

Marco-Tulio Fonseca Rodrigues – *Chemical Sciences and Engineering Division, Argonne National Laboratory, Lemont, Illinois 60439, United States;* orcid.org/0000-0003-0833-6556

Stephen E. Trask – *Chemical Sciences and Engineering Division, Argonne National Laboratory, Lemont, Illinois 60439, United States;* orcid.org/0000-0002-0879-4779

Andrew M. Colclasure – *Chemical Sciences and Engineering Division, Argonne National Laboratory, Lemont, Illinois 60439, United States;* orcid.org/0000-0002-9574-5106

Kristin A. Persson – *Department of Materials Science and Engineering, University of California Berkeley, Berkeley, California 94720, United States; Materials Science Division, Lawrence Berkeley National Laboratory, Berkeley, California 94720, United States;* orcid.org/0000-0003-2495-5509

Complete contact information is available at: https://pubs.acs.org/doi/10.1021/acsami.5c23255

Author Contributions

The manuscript was written through contributions of all authors. All authors have given approval to the final version of the manuscript.

Notes

The authors declare no competing financial interest.

■ ACKNOWLEDGMENTS

This research was supported by the U.S. Department Office of Critical Minerals and Energy Innovation (CMEI), Battery R&D, directed by Carine Steinway, Nicolas Edison, Thomas Do, and Brian Cunningham and managed by Anthony Burrell. This manuscript has been authored in part by UT-Battelle, LLC, under contract DE-AC05-00OR22725 with the US Department of Energy (DOE). The publisher, by accepting the article for publication, acknowledges that the US government retains a nonexclusive, paid-up, irrevocable, worldwide license to publish or reproduce the published form of this manuscript, or allow others to do so, for US government purposes.

Downloaded from pubs.acs.org/aamick/article-pdf/18/38/52238/6858050/am-2025-23255a.pdf by LAWRENCE BERKELEY NATL LABORATORY user on 06 November 2026

DOE will provide public access to these results of federally sponsored research in accordance with the DOE Public Access Plan (http://energy.gov/downloads/doepublic-accessplan). Argonne National Laboratory ("Argonne") is operated by UChicago Argonne LLC, and is a U.S. Department of Energy Office of Science laboratory, operated under Contract No. DE-AC02-06CH11357. National Laboratory of the Rockies, operated by Alliance for Energy Innovation, LLC, for the US Department of Energy (DOE) under Contract No. DE-AC36-08GO28308. Idaho National laboratory is operated by Battelle Energy Alliance, LLC under Contract No. DE-AC07-05ID14517 with the U.S. Department of Energy. We acknowledge the use of Copilot (https://copilot.microsoft.com/) to generate images of lemmings with varying facial expressions for use within the table of contents. The initial prompt was "Can you make me an image of a lithiated silicon as a lemming? This is for a graphical abstract." The following prompts were then adapted to generate lemmings with different facial expressions.

REFERENCES

(1) Zhang, Y.; Zhu, Y.; Fu, L.; Meng, J.; Yu, N.; Wang, J.; Wu, Y. Si/C Composites as Negative Electrode for High Energy Lithium Ion Batteries. *Chin. J. Chem.* **2017**, *35* (1), 21−29.

(2) McBrayer, J. D.; Rodrigues, M.-T. F.; Schulze, M. C.; Abraham, D. P.; Apblett, C. A.; Bloom, I.; Carroll, G. M.; Colclasure, A. M.; Fang, C.; Harrison, K. L.; Liu, G.; Minteer, S. D.; Neale, N. R.; Veith, G. M.; Johnson, C. S.; Vaughey, J. T.; Burrell, A. K.; Cunningham, B. Calendar Aging of Silicon-Containing Batteries. *Nat. Energy* **2021**, *6* (9), 866−872.

(3) Dubarry, M.; Qin, N.; Brooker, P. Calendar Aging of Commercial Li-Ion Cells of Different Chemistries − A Review. *Curr. Opin. Electrochem.* **2018**, *9*, 106−113.

(4) McBrayer, J. D.; Harrison, K. L.; Allcorn, E.; Minteer, S. D. Chemical Contributions to Silicon Anode Calendar Aging Are Dominant over Mechanical Contributions. *Front. Batter. Electrochem.* **2023**, *2*, No. 1308127.

(5) Wood, K. N.; Teeter, G. XPS on Li-Battery-Related Compounds: Analysis of Inorganic SEI Phases and a Methodology for Charge Correction. *ACS Appl. Energy Mater.* **2018**, *1* (9), 4493−4504.

(6) Araño, K. G.; Armstrong, B. L.; Yang, G.; Kumara, C.; Ward, T. Z.; Meyer, H. M. I.; Rogers, A. M.; Toups, E.; Veith, G. M. Elucidating the Role of Carbon Conductive Additive in the Processing and Electrochemical Behavior of Surface-Modified Si Anodes. *Energy Fuels* **2024**, *38* (7), 6446−6458.

(7) Casino, S.; Beuse, T.; Küpers, V.; Börner, M.; Gallasch, T.; Winter, M.; Niehoff, P. Quantification of Aging Mechanisms of Carbon-Coated and Uncoated Silicon Thin Film Anodes in Lithium Metal and Lithium Ion Cells. *J. Energy Storage* **2021**, *41*, No. 102812.

(8) Zhan, Q.; Zhao, Z.; Fan, X.; Xu, T.; Li, F.; Qi, J.; Li, H.; Guo, Y.; Zhang, X.; Zhou, Z.; Wu, S.; Yang, Q.-H. Beyond Mechanics: Inherently HF-Phobic Si with Minimized Corrosion for Stable Li Storage. *Adv. Energy Mater.* **2025**, *15* (31), No. 2501679.

(9) Grill, J.; Popovic-Neuber, J. Long Term Porosity of Solid Electrolyte Interphase on Model Silicon Anodes with Liquid Battery Electrolytes. *Commun. Chem.* **2024**, *7* (1).

(10) von Kolzenberg, L.; Latz, A.; Horstmann, B. Chemo-Mechanical Model of SEI Growth on Silicon Electrode Particles. *Batteries Supercaps* **2022**, *5* (2), No. e202100216.

(11) Di Muzio, S.; Paolone, A.; Brutti, S. Thermodynamics of the Hydrolysis of Lithium Salts: Pathways to the Precipitation of Inorganic SEI Components in Li-Ion Batteries. *J. Electrochem. Soc.* **2021**, *168* (10), No. 100514.

(12) Lux, S. F.; Lucas, I. T.; Pollak, E.; Passerini, S.; Winter, M.; Kostecki, R. The Mechanism of HF Formation in LiPF6 Based Organic Carbonate Electrolytes. *Electrochem. Commun.* **2012**, *14* (1), 47−50.

(13) Ha, Y.; Stetson, C.; Harvey, S. P.; Teeter, G.; Tremolet de Villers, B. J.; Jiang, C.-S.; Schnabel, M.; Stradins, P.; Burrell, A.; Han, S.-D. Effect of Water Concentration in $LiPF_6$-Based Electrolytes on the Formation, Evolution, and Properties of the Solid Electrolyte Interphase on Si Anodes. *ACS Appl. Mater. Interfaces* **2020**, *12* (44), 49563−49573.

(14) Rodrigues, M.-T. F.; Yang, Z.; Trask, S. E.; Dunlop, A. R.; Kim, M.; Dogan, F.; Key, B.; Bloom, I.; Abraham, D. P.; Jansen, A. N. Pouch Cells with 15% Silicon Calendar-Aged for 4 Years. *J. Power Sources* **2023**, *565*, No. 232894.

(15) Terborg, L.; Nowak, S.; Passerini, S.; Winter, M.; Karst, U.; Haddad, P. R.; Nesterenko, P. N. Ion Chromatographic Determination of Hydrolysis Products of Hexafluorophosphate Salts in Aqueous Solution. *Anal. Chim. Acta* **2012**, *714*, 121−126.

(16) Stich, M.; Göttlinger, M.; Kurniawan, M.; Schmidt, U.; Bund, A. Hydrolysis of LiPF6 in Carbonate-Based Electrolytes for Lithium-Ion Batteries and in Aqueous Media. *J. Phys. Chem. C* **2018**, *122* (16), 8836−8842.

(17) Yin, Y.; Arca, E.; Wang, L.; Yang, G.; Schnabel, M.; Cao, L.; Xiao, C.; Zhou, H.; Liu, P.; Nanda, J.; Teeter, G.; Eichhorn, B.; Xu, K.; Burrell, A.; Ban, C. Nonpassivated Silicon Anode Surface. *ACS Appl. Mater. Interfaces* **2020**, *12* (23), 26593−26600.

(18) Sayavong, P.; Zhang, W.; Oyakhire, S. T.; Boyle, D. T.; Chen, Y.; Kim, S. C.; Vilá, R. A.; Holmes, S. E.; Kim, M. S.; Bent, S. F.; Bao, Z.; Cui, Y. Dissolution of the Solid Electrolyte Interphase and Its Effects on Lithium Metal Anode Cyclability. *J. Am. Chem. Soc.* **2023**, *145* (22), 12342−12350.

(19) Wood, S. M.; Fang, C.; Dufek, E. J.; Nagpure, S. C.; Sazhin, S. V.; Liaw, B.; Meng, Y. S. Predicting Calendar Aging in Lithium Metal Secondary Batteries: The Impacts of Solid Electrolyte Interphase Composition and Stability. *Adv. Energy Mater.* **2018**, *8* (26), No. 1801427.

(20) Tasaki, K.; Harris, S. J. Computational Study on the Solubility of Lithium Salts Formed on Lithium Ion Battery Negative Electrode in Organic Solvents. *J. Phys. Chem. C* **2010**, *114* (17), 8076−8083.

(21) Tasaki, K.; Goldberg, A.; Lian, J.-J.; Walker, M.; Timmons, A.; Harris, S. J. Solubility of Lithium Salts Formed on the Lithium-Ion Battery Negative Electrode Surface in Organic Solvents. *J. Electrochem. Soc.* **2009**, *156* (12), No. A1019.

(22) Verma, A.; Schulze, M. C.; Colclasure, A.; Rodrigues, M.-T. F.; Trask, S. E.; Pupek, K.; Abraham, D. P. Significant Improvements to Si Calendar Lifetime Using Rapid Electrolyte Screening via Potentiostatic Holds. *J. Electrochem. Soc.* **2024**, *171* (7), No. 070539.

(23) Schulze, M. C.; Rodrigues, M.-T. F.; McBrayer, J. D.; Abraham, D. P.; Apblett, C. A.; Bloom, I.; Chen, Z.; Colclasure, A. M.; Dunlop, A. R.; Fang, C.; Harrison, K. L.; Liu, G.; Minteer, S. D.; Neale, N. R.; Robertson, D.; Tornheim, A. P.; Trask, S. E.; Veith, G. M.; Verma, A.; Yang, Z.; Johnson, C. Critical Evaluation of Potentiostatic Holds as Accelerated Predictors of Capacity Fade during Calendar Aging. *J. Electrochem. Soc.* **2022**, *169* (5), No. 050531.

(24) Verma, A.; Schulze, M. C.; Colclasure, A.; Rodrigues, M.-T. F.; Trask, S. E.; Pupek, K.; Johnson, C. S.; Abraham, D. P. Assessing Electrolyte Fluorination Impact on Calendar Aging of Blended Silicon-Graphite Lithium-Ion Cells Using Potentiostatic Holds. *J. Electrochem. Soc.* **2023**, *170* (7), No. 070516.

(25) Malkowski, T. F.; Yang, Z.; Sacci, R. L.; Trask, S. E.; Rodrigues, M.-T. F.; Bloom, I. D.; Veith, G. M. Evaluating the Roles of Electrolyte Components on the Passivation of Silicon Anodes. *J. Power Sources* **2022**, *523*, No. 231021.

(26) Quinn, J.; Kim, J.-M.; Yi, R.; Zhang, J.-G.; Xiao, J.; Wang, C. Fluoro-Ethylene-Carbonate Plays a Double-Edged Role on the Stability of Si Anode-Based Rechargeable Batteries During Cycling and Calendar Aging. *Adv. Mater.* **2024**, *36* (30), No. 2402625.

(27) Johnson, N. M.; Yang, Z.; Liu, Q.; Zhang, Z. Enabling Non-Carbonate Electrolytes for Silicon Anode Batteries Using Fluoroethylene Carbonate. *J. Electrochem. Soc.* **2022**, *169* (4), No. 040527.

Downloaded from pubs.acs.org/aamick/article-pdf/18/38/52238/6858050/am-2025-23255a.pdf by LAWRENCE BERKELEY NATL LABORATORY user on 06 November 2026

https://doi.org/10.1021/acsami.5c23255
ACS Appl. Mater. Interfaces 2026, 18, 52238−52252

(28) Gao, N.; Kim, S.; Chinnam, P.; Dufek, E. J.; Colclasure, A. M.; Jansen, A.; Son, S.-B.; Bloom, I.; Dunlop, A.; Trask, S.; Gering, K. L. Methodologies for Design, Characterization and Testing of Electrolytes That Enable Extreme Fast Charging of Lithium-Ion Cells. *Energy Storage Mater.* **2022**, *44*, 296−312.
(29) Lee, K.-K.; Park, K.; Lee, H.; Noh, Y.; Kossowska, D.; Kwak, K.; Cho, M. Ultrafast Fluxional Exchange Dynamics in Electrolyte Solvation Sheath of Lithium Ion Battery. *Nat. Commun.* **2017**, *8* (1), No. 14658.
(30) Hou, T.; Yang, G.; Rajput, N. N.; Self, J.; Park, S.-W.; Nanda, J.; Persson, K. A. The Influence of FEC on the Solvation Structure and Reduction Reaction of $LiPF_6$/EC Electrolytes and Its Implication for Solid Electrolyte Interphase Formation. *Nano Energy* **2019**, *64*, No. 103881.
(31) Hou, T.; Fong, K. D.; Wang, J.; Persson, K. A. The Solvation Structure, Transport Properties and Reduction Behavior of Carbonate-Based Electrolytes of Lithium-Ion Batteries. *Chem. Sci.* **2021**, *12* (44), 14740−14751.
(32) He, J.; Wang, H.; Zhou, Q.; Qi, S.; Wu, M.; Li, F.; Hu, W.; Ma, J. Unveiling the Role of Li^+ Solvation Structures with Commercial Carbonates in the Formation of Solid Electrolyte Interphase for Lithium Metal Batteries. *Small Methods* **2021**, *5* (8), No. 2100441.
(33) Woods, E. F.; Wu, D.; Robertson, L. A.; Liu, H.; Key, B.; Vaughey, J. T.; Zhang, Z. Electrolyte Design for Silicon-Based Li-Ion Battery Guided by Chemical Reactivity of Solvents with a Model Silicon Anode. *ACS Appl. Energy Mater.* **2024**, *7* (19), 8294−8300.
(34) Aurbach, D.; Gamolsky, K.; Markovsky, B.; Gofer, Y.; Schmidt, M.; Heider, U. On the Use of Vinylene Carbonate (VC) as an Additive to Electrolyte Solutions for Li-Ion Batteries. *Electrochim. Acta* **2002**, *47* (9), 1423−1439.
(35) Rodrigues, M.-T. F.; Trask, S. E.; Dunlop, A. R.; Lan, Y.-C.; Kubal, J.; Salpekar, D.; Prado, A. Y. R.; Wang, E.; McDaniel, C.; Woods, E. F.; Robertson, L. A.; Tancin, R. J.; Schulze, M. C.; Folastre, N.; Key, B.; Zhang, Z.; Lu, W.; Abraham, D. P.; Jansen, A. N. Building High-Energy Silicon-Containing Batteries Using Off-The-Shelf Materials. *J. Electrochem. Soc.* **2025**, *172* (12), No. 120521.
(36) Geuder, K.; Klick, S.; Finster, P.; Graff, K. M.; Winter, M.; Nowak, S.; Seifert, H. J.; Ziebert, C. Influence of Vinylene Carbonate and Fluoroethylene Carbonate on Open Circuit and Floating SoC Calendar Aging of Lithium-Ion Batteries. *Batteries* **2024**, *10* (8), No. 275.
(37) Michan, A. L.; Parimalam, B. S.; Leskes, M.; Kerber, R. N.; Yoon, T.; Grey, C. P.; Lucht, B. L. Fluoroethylene Carbonate and Vinylene Carbonate Reduction: Understanding Lithium-Ion Battery Electrolyte Additives and Solid Electrolyte Interphase Formation. *Chem. Mater.* **2016**, *28* (22), 8149−8159.
(38) Burns, J. C.; Petibon, R.; Nelson, K. J.; Sinha, N. N.; Kassam, A.; Way, B. M.; Dahn, J. R. Studies of the Effect of Varying Vinylene Carbonate (VC) Content in Lithium Ion Cells on Cycling Performance and Cell Impedance. *J. Electrochem. Soc.* **2013**, *160* (10), No. A1668.
(39) Lechtenfeld, C.-T.; Buchmann, J.; Hagemeister, J.; Bela, M. M.; van Wickeren, S.; Stock, S.; Daub, R.; Wiemers-Meyer, S.; Winter, M.; Nowak, S. Analyzing the Effect of Electrolyte Quantity on the Aging of Lithium-Ion Batteries. *Adv. Sci.* **2024**, *11* (39), No. 2405897.
(40) Attia, P. M.; Chueh, W. C.; Harris, S. J. Revisiting the $T^{0.5}$ Dependence of SEI Growth. *J. Electrochem. Soc.* **2020**, *167* (9), No. 090535.
(41) von Kolzenberg, L.; Latz, A.; Horstmann, B. Solid−Electrolyte Interphase During Battery Cycling: Theory of Growth Regimes. *ChemSusChem* **2020**, *13* (15), 3901−3910.
(42) Eastman, P.; Galvelis, R.; Peláez, R. P.; Abreu, C. R. A.; Farr, S. E.; Gallicchio, E.; Gorenko, A.; Henry, M. M.; Hu, F.; Huang, J.; Krämer, A.; Michel, J.; Mitchell, J. A.; Pande, V. S.; Rodrigues, J. P.; Rodriguez-Guerra, J.; Simmonett, A. C.; Singh, S.; Swails, J.; Turner, P.; Wang, Y.; Zhang, I.; Chodera, J. D.; De Fabritiis, G.; Markland, T. E. OpenMM 8: Molecular Dynamics Simulation with Machine Learning Potentials. *J. Phys. Chem. B* **2024**, *128* (1), 109−116.
(43) Ganose, A. M.; Sahasrabuddhe, H.; Asta, M.; Beck, K.; Biswas, T.; Bonkowski, A.; Bustamante, J.; Chen, X.; Chiang, Y.; Chrzan, D. C.; Clary, J.; Cohen, O. A.; Ertural, C.; Gallant, M. C.; George, J.; Gerits, S.; Goodall, R. E. A.; Guha, R. D.; Hautier, G.; Horton, M.; Inizan, T. J.; Kaplan, A. D.; Kingsbury, R. S.; Kuner, M. C.; Li, B.; Linn, X.; McDermott, M. J.; Mohanakrishnan, R. S.; Naik, A. N.; Neaton, J. B.; Parmar, S. M.; Persson, K. A.; Petretto, G.; Purcell, T. A. R.; Ricci, F.; Rich, B.; Riebesell, J.; Rignanese, G.-M.; Rosen, A. S.; Scheffler, M.; Schmidt, J.; Shen, J.-X.; Sobolev, A.; Sundararaman, R.; Tezak, C.; Trinquet, V.; Varley, J. B.; Vigil-Fowler, D.; Wang, D.; Waroquiers, D.; Wen, M.; Yang, H.; Zheng, H.; Zheng, J.; Zhu, Z.; Jain, A. Atomate2: Modular Workflows for Materials Science. *Digit. Discov.* **2025**, *4* (7), 1944−1973.
(44) Boothroyd, S.; Behara, P. K.; Madin, O. C.; Hahn, D. F.; Jang, H.; Gapsys, V.; Wagner, J. R.; Horton, J. T.; Dotson, D. L.; Thompson, M. W.; Maat, J.; Gokey, T.; Wang, L.-P.; Cole, D. J.; Gilson, M. K.; Chodera, J. D.; Bayly, C. I.; Shirts, M. R.; Mobley, D. L. Development and Benchmarking of Open Force Field 2.0.0: The Sage Small Molecule Force Field. *J. Chem. Theory Comput.* **2023**, *19* (11), 3251−3275.
(45) Epifanovsky, E.; Gilbert, A. T. B.; Feng, X.; Lee, J.; Mao, Y.; Mardirossian, N.; Pokhilko, P.; White, A. F.; Coons, M. P.; Dempwolff, A. L.; Gan, Z.; Hait, D.; Horn, P. R.; Jacobson, L. D.; Kaliman, I.; Kussmann, J.; Lange, A. W.; Lao, K. U.; Levine, D. S.; Liu, J.; McKenzie, S. C.; Morrison, A. F.; Nanda, K. D.; Plasser, F.; Rehn, D. R.; Vidal, M. L.; You, Z.-Q.; Zhu, Y.; Alam, B.; Albrecht, B. J.; Aldossary, A.; Alguire, E.; Andersen, J. H.; Athavale, V.; Barton, D.; Begam, K.; Behn, A.; Bellonzi, N.; Bernard, Y. A.; Berquist, E. J.; Burton, H. G. A.; Carreras, A.; Carter-Fenk, K.; Chakraborty, R.; Chien, A. D.; Closser, K. D.; Cofer-Shabica, V.; Dasgupta, S.; De Wergifosse, M.; Deng, J.; Diedenhofen, M.; Do, H.; Ehlert, S.; Fang, P.-T.; Fatehi, S.; Feng, Q.; Friedhoff, T.; Gayvert, J.; Ge, Q.; Gidofalvi, G.; Goldey, M.; Gomes, J.; González-Espinoza, C. E.; Gulania, S.; Gunina, A. O.; Hanson-Heine, M. W. D.; Harbach, P. H. P.; Hauser, A.; Herbst, M. F.; Hernández Vera, M.; Hodecker, M.; Holden, Z. C.; Houck, S.; Huang, X.; Hui, K.; Huynh, B. C.; Ivanov, M.; Jász, Á.; Ji, H.; Jiang, H.; Kaduk, B.; Kähler, S.; Khistyaev, K.; Kim, J.; Kis, G.; Klunzinger, P.; Koczor-Benda, Z.; Koh, J. H.; Kosenkov, D.; Koulias, L.; Kowalczyk, T.; Krauter, C. M.; Kue, K.; Kunitsa, A.; Kus, T.; Ladjánszki, I.; Landau, A.; Lawler, K. V.; Lefrancois, D.; Lehtola, S.; Li, R. R.; Li, Y.-P.; Liang, J.; Liebenthal, M.; Lin, H.-H.; Lin, Y.-S.; Liu, F.; Liu, K.-Y.; Loipersberger, M.; Luenser, A.; Manjanath, A.; Manohar, P.; Mansoor, E.; Manzer, S. F.; Mao, S.-P.; Marenich, A. V.; Markovich, T.; Mason, S.; Maurer, S. A.; McLaughlin, P. F.; Menger, M. F. S. J.; Mewes, J.-M.; Mewes, S. A.; Morgante, P.; Mullinax, J. W.; Oosterbaan, K. J.; Paran, G.; Paul, A. C.; Paul, S. K.; Pavošević, F.; Pei, Z.; Prager, S.; Proynov, E. I.; Rák, Á.; Ramos-Cordoba, E.; Rana, B.; Rask, A. E.; Rettig, A.; Richard, R. M.; Rob, F.; Rossomme, E.; Scheele, T.; Scheurer, M.; Schneider, M.; Sergueev, N.; Sharada, S. M.; Skomorowski, W.; Small, D. W.; Stein, C. J.; Su, Y.-C.; Sundstrom, E. J.; Tao, Z.; Thirman, J.; Tornai, G. J.; Tsuchimochi, T.; Tubman, N. M.; Veccham, S. P.; Vydrov, O.; Wenzel, J.; Witte, J.; Yamada, A.; Yao, K.; Yeganeh, S.; Yost, S. R.; Zech, A.; Zhang, I. Y.; Zhang, X.; Zhang, Y.; Zuev, D.; Aspuru-Guzik, A.; Bell, A. T.; Besley, N. A.; Bravaya, K. B.; Brooks, B. R.; Casanova, D.; Chai, J.-D.; Coriani, S.; Cramer, C. J.; Cserey, G.; DePrince, A. E.; DiStasio, R. A.; Dreuw, A.; Dunietz, B. D.; Furlani, T. R.; Goddard, W. A.; Hammes-Schiffer, S.; Head-Gordon, T.; Hehre, W. J.; Hsu, C.-P.; Jagau, T.-C.; Jung, Y.; Klamt, A.; Kong, J.; Lambrecht, D. S.; Liang, W.; Mayhall, N. J.; McCurdy, C. W.; Neaton, J. B.; Ochsenfeld, C.; Parkhill, J. A.; et al. Software for the Frontiers of Quantum Chemistry: An Overview of Developments in the Q-Chem 5 Package. *J. Chem. Phys.* **2021**, *155* (8), No. 084801.
(46) Chaudhari, M. I.; Nair, J. R.; Pratt, L. R.; Soto, F. A.; Balbuena, P. B.; Rempe, S. B. Scaling Atomic Partial Charges of Carbonate

Downloaded from pubs.acs.org/aamick/article-pdf/18/38/52238/6858305O/am-2025-23255a.pdf by LAWRENCE BERKELEY NATL LABORATORY user on 06 November 2026

https://doi.org/10.1021/acsami.5c23255
ACS Appl. Mater. Interfaces 2026, 18, 52238−52252

Solvents for Lithium Ion Solvation and Diffusion. *J. Chem. Theory Comput.* **2016**, *12* (12), 5709−5718.
(47) Leontyev, I.; Stuchebrukhov, A. Accounting for Electronic Polarization in Non-Polarizable Force Fields. *Phys. Chem. Chem. Phys.* **2011**, *13* (7), 2613−2626.
(48) Martínez, L.; Andrade, R.; Birgin, E. G.; Martínez, J. M. PACKMOL: A Package for Building Initial Configurations for Molecular Dynamics Simulations. *J. Comput. Chem.* **2009**, *30* (13), 2157−2164.
(49) Cohen, O. A.; Macdermott-Opeskin, H.; Lee, L.; Hou, T.; Fong, K. D.; Kingsbury, R.; Wang, J.; Persson, K. A. SolvationAnalysis: A Python Toolkit for Understandingliquid Solvation Structure in Classical Molecular Dynamics simulations. *JOSS* **2023**, *8* (84), No. 5183.
(50) Gowers, R.; Linke, M.; Barnoud, J.; Reddy, T.; Melo, M.; Seyler, S.; Domański, J.; Dotson, D.; Buchoux, S.; Kenney, I.; Beckstein, O.MDAnalysis: A Python Package for the Rapid Analysis of Molecular Dynamics Simulations. In *Proceedings of the 15th Python in Science Conference*, Austin, Texas, July 2016; SciPy: Austin, Texas, **2016**; pp 98−105.
(51) Michaud-Agrawal, N.; Denning, E. J.; Woolf, T. B.; Beckstein, O. MDAnalysis: A Toolkit for the Analysis of Molecular Dynamics Simulations. *J. Comput. Chem.* **2011**, *32* (10), 2319−2327.
(52) Gering, K. L. Prediction of Electrolyte Viscosity for Aqueous and Non-Aqueous Systems: Results from a Molecular Model Based on Ion Solvation and a Chemical Physics Framework. *Electrochim. Acta* **2006**, *51* (15), 3125−3138.
(53) Gering, K. L. Prediction of Electrolyte Conductivity: Results from a Generalized Molecular Model Based on Ion Solvation and a Chemical Physics Framework. *Electrochim. Acta* **2017**, *225*, 175−189.
(54) Logan, E. R.; Gering, K. L.; Ma, X.; Dahn, J. Electrolyte Development for High-Performance Li-Ion Cells: Additives, Solvents, and Agreement with a Generalized Molecular Model. *Electrochem. Soc. Interface* **2019**, *28* (2), 49.
(55) Schulze, M. C.; Prakash, N.; Gering, K.; Colclasure, A. M.; Weddle, P. J. Predicting Si-Anode Calendar Life Using Machine Learning: Correlating Electrolyte Properties and Electrochemical Signals. *J. Power Sources* **2025**, *659*, No. 238338.
(56) Borodin, O.; Self, J.; Persson, K. A.; Wang, C.; Xu, K. Uncharted Waters: Super-Concentrated Electrolytes. *Joule* **2020**, *4* (1), 69−100.
(57) Giffin, G. A. The Role of Concentration in Electrolyte Solutions for Non-Aqueous Lithium-Based Batteries. *Nat. Commun.* **2022**, *13* (1), No. 5250.
(58) Shim, Y. Computer Simulation Study of the Solvation of Lithium Ions in Ternary Mixed Carbonate Electrolytes: Free Energetics, Dynamics, and Ion Transport. *Phys. Chem. Chem. Phys.* **2018**, *20* (45), 28649−28657.
(59) Chen, X.; Zhang, Q. Atomic Insights into the Fundamental Interactions in Lithium Battery Electrolytes. *Acc. Chem. Res.* **2020**, *53* (9), 1992−2002.
(60) Berman, H. A.; Stengle, T. R. Contact Ion Pairing of the Perchlorate Ion. Chlorine-35 Nuclear Magnetic Resonance Study. I Solutions in Pure Solvents. *J. Phys. Chem.* **1975**, *79* (10), 1001−1005.
(61) Su, C.-C.; He, M.; Amine, R.; Chen, Z.; Amine, K. The Relationship between the Relative Solvating Power of Electrolytes and Shuttling Effect of Lithium Polysulfides in Lithium−Sulfur Batteries. *Angew. Chem., Int. Ed.* **2018**, *57* (37), 12033−12036.
(62) Shterenberg, I.; Salama, M.; Gofer, Y.; Aurbach, D. X-Ray Photodecomposition of Bis(Trifluoromethanesulfonyl)Imide, Bis(Fluorosulfonyl)Imide, and Hexafluorophosphate. *J. Phys. Chem. C* **2017**, *121* (7), 3744−3751.
(63) Yu, W.; Yu, Z.; Cui, Y.; Bao, Z. Degradation and Speciation of Li Salts during XPS Analysis for Battery Research. *ACS Energy Lett.* **2022**, *7* (10), 3270−3275.
(64) Aupperle, F.; Von Aspern, N.; Berghus, D.; Weber, F.; Eshetu, G. G.; Winter, M.; Figgemeier, E. The Role of Electrolyte Additives on the Interfacial Chemistry and Thermal Reactivity of Si-Anode-Based Li-Ion Battery. *ACS Appl. Energy Mater.* **2019**, *2* (9), 6513−6527.
(65) Schroder, K. W.; Celio, H.; Webb, L. J.; Stevenson, K. J. Examining Solid Electrolyte Interphase Formation on Crystalline Silicon Electrodes: Influence of Electrochemical Preparation and Ambient Exposure Conditions. *J. Phys. Chem. C* **2012**, *116* (37), 19737−19747.
(66) Jin, Y.; Kneusels, N.-J. H.; Marbella, L. E.; Castillo-Martínez, E.; Magusin, P. C. M. M.; Weatherup, R. S.; Jónsson, E.; Liu, T.; Paul, S.; Grey, C. P. Understanding Fluoroethylene Carbonate and Vinylene Carbonate Based Electrolytes for Si Anodes in Lithium Ion Batteries with NMR Spectroscopy. *J. Am. Chem. Soc.* **2018**, *140* (31), 9854−9867.
(67) Gogoi, N.; Lundström, R.; Hernández, G.; Berg, E. J. Base-Driven Ring-Opening Reactions of Vinylene Carbonate. *J. Electrochem. Soc.* **2024**, *171* (5), No. 050506.
(68) Sloop, S. E.; Pugh, J. K.; Wang, S.; Kerr, J. B.; Kinoshita, K. Chemical Reactivity of PF 5 and LiPF6 in Ethylene Carbonate/Dimethyl Carbonate Solutions. *Electrochem. Solid-State Lett.* **2001**, *4* (4), A42.
(69) Kawamura, T.; Okada, S.; Yamaki, J. Decomposition Reaction of $LiPF_6$-Based Electrolytes for Lithium Ion Cells. *J. Power Sources* **2006**, *156* (2), 547−554.
(70) Park, S.; Jeong, S. Y.; Lee, T. K.; Park, M. W.; Lim, H. Y.; Sung, J.; Cho, J.; Kwak, S. K.; Hong, S. Y.; Choi, N.-S. Replacing Conventional Battery Electrolyte Additives with Dioxolone Derivatives for High-Energy-Density Lithium-Ion Batteries. *Nat. Commun.* **2021**, *12* (1), No. 838.
(71) Lam, S.; Verma, A.; Schulze, M. C.; Sacci, R. L.; Meyer, H. M. III; Lance, M. J.; Araño, K. G.; Musgrove, A. L.; Fonseca Rodrigues, M.-T.; Trask, S. E.; Colclasure, A.; Veith, G. M. Surprising Relationship between Silicon Anode Calendar Aging and Electrolyte Components in a Localized High-Concentration Electrolyte System. *ACS Appl. Mater. Interfaces* **2025**, *17* (30), 43020−43033.
(72) Han, H.-B.; Zhou, S.-S.; Zhang, D.-J.; Feng, S.-W.; Li, L.-F.; Liu, K.; Feng, W.-F.; Nie, J.; Li, H.; Huang, X.-J.; Armand, M.; Zhou, Z.-B. Lithium Bis(Fluorosulfonyl)Imide (LiFSI) as Conducting Salt for Nonaqueous Liquid Electrolytes for Lithium-Ion Batteries: Physicochemical and Electrochemical Properties. *J. Power Sources* **2011**, *196* (7), 3623−3632.
(73) McBrayer, J. D.; Apblett, C. A.; Harrison, K. L.; Fenton, K. R.; Minteer, S. D. Mechanical Studies of the Solid Electrolyte Interphase on Anodes in Lithium and Lithium Ion Batteries. *Nanotechnology* **2021**, *32* (50), No. 502005.
(74) Gao, A.; Lai, H.; Duan, M.; Chen, S.; Huang, W.; Yang, M.; Gong, L.; Chen, J.; Xie, F.; Meng, H. LiF Artifacts in XPS Analysis of the SEI for Lithium Metal Batteries. *ACS Appl. Mater. Interfaces* **2025**, *17* (5), 8513−8525.
(75) Freiberg, A. T. S.; Sicklinger, J.; Solchenbach, S.; Gasteiger, H. A. Li_2CO_3 Decomposition in Li-Ion Batteries Induced by the Electrochemical Oxidation of the Electrolyte and of Electrolyte Impurities. *Electrochim. Acta* **2020**, *346*, No. 136271.
(76) Ren, X.; Chen, S.; Lee, H.; Mei, D.; Engelhard, M. H.; Burton, S. D.; Zhao, W.; Zheng, J.; Li, Q.; Ding, M. S.; Schroeder, M.; Alvarado, J.; Xu, K.; Meng, Y. S.; Liu, J.; Zhang, J.-G.; Xu, W. Localized High-Concentration Sulfone Electrolytes for High-Efficiency Lithium-Metal Batteries. *Chem* **2018**, *4* (8), 1877−1892.
(77) Tanaka, S.; Taniguchi, M.; Tanigawa, H. XPS and UPS Studies on Electronic Structure of Li_2O *J. Nucl. Mater.* **2000**, *283*−*287*, 1405−1408.
(78) Hall, D. S.; Self, J.; Dahn, J. R. Dielectric Constants for Quantum Chemistry and Li-Ion Batteries: Solvent Blends of Ethylene Carbonate and Ethyl Methyl Carbonate. *J. Phys. Chem. C* **2015**, *119* (39), 22322−22330.
(79) Wang, Y.; Nakamura, S.; Tasaki, K.; Balbuena, P. B. Theoretical Studies To Understand Surface Chemistry on Carbon Anodes for Lithium-Ion Batteries: How Does Vinylene Carbonate Play Its Role as an Electrolyte Additive? *J. Am. Chem. Soc.* **2002**, *124* (16), 4408−4421.

Downloaded from pubs.acs.org/aamick/article-pdf/18/38/52238/6858050/am-2025-23255a.pdf by LAWRENCE BERKELEY NATL LABORATORY user on 06 November 2026

https://doi.org/10.1021/acsami.5c23255
ACS Appl. Mater. Interfaces 2026, 18, 52238−52252